Investigation of Image Characteristics in Super-resolution Microsphere Nanoscope

A thesis submitted to The University of Manchester for the degree of
Master of Philosophy
in the Faculty of Engineering and Physical Sciences

2016

Wenxuan Shi

School of Mechanical, Aerospace and Civil Engineering

LIST OF CONTENTS

Chapter Page

Word Count:16,725

LIST OF FIGURES AND TABLES

Figure Page

LIST OF ABBREVIATIONS

FWHM	full width at half maximum
STED	stimulated emission depletion microscopy
MONS	microsphere optical nanoscopy
NSOM	near-field scanning optical microscopy
TIRF	total internal reflection fluorescence
HF	hydrofluoric acid
SMON	submerged microsphere optical nanoscopy
EM	electromagnetic
PS	polystyrene microsphere
GO	geometrical optics
BTG	barium titanate glass
IPA	isopropyl alcohol
PSF	point spread function
NPD	nanoparticle dimers
2-D	two dimension
3-D	three dimension
NA	numerical aperture
SEM	scanning electron microscopy

LIST OF SYMBOLS

Roman Symbols

a_n	expansion coefficients in Mie theory [a.u.]
b_n	expansion coefficients in Mie theory [a.u.]
c_n	expansion coefficients in Mie theory [a.u.]
d_n	expansion coefficients in Mie theory [a.u.]
d	distance of two point sources [m]
E_0	amplitude of the electric field [V/m]
$\vec{E}_i$	incident electric field [V/m]
$\vec{E}_1$	internal electric field [V/m]
$\vec{E}_s$	scattered electric field [V/m]
f	focal length of the microsphere from the sphere center [m]
f_{Mie}	focal length in Mie theory [m]
f_{GO}	focal length in Geometrical optics [m]
$\vec{H}_i$	incident magnetic field [A/m^2]
$\vec{H}_1$	internal magnetic field [A/m^2]
$\vec{H}_s$	scattered magnetic field [A/m^2]
$h_n^{(1)}(kR)$	Hankel functions of the first kind [a.u.]
$h_n^{(2)}(kR)$	Hankel functions of the second kind [a.u.]
I_i	intensity of incident light [W/m^2]
I_s	intensity of scattered light [W/m^2]
$j_n(kR)$	spherical Bessel functions [a.u.]
k	wave number [m^{-1}]
l	transverse distance from the optical axis [m]
l'	imaging plane position from the center of the microsphere[m]
m	refractive index [a.u.]
$\vec{M}_{mn}$	vector spherical wave functions [a.u.]
$\vec{N}_{mn}$	vector spherical wave functions [a.u.]
$P_n^m(\cos\theta)$	Legendre functions of the first kind [a.u.]
$\vec{r}$	radius vector [m]
R	radius of microsphere [m]
x	size parameter of microsphere [a.u.]
x_d	original (distorted) point of image in x coordinates [a.u.]
x_u	corrected (undistorted) point of image in x coordinates [a.u.]

x_c	center point of the image in x coordinates [a.u.]
y_d	original (distorted) point of image in y coordinates [a.u.]
y_u	corrected (undistorted) point of image in y coordinates [a.u.]
y_c	center point of the image in y coordinates [a.u.]
$y_n(kR)$	Neumann functions [a.u.]
$z_n(kR)$	any of the four spherical Bessel functions [a.u.]

Greek symbols

β	microsphere image magnification factor [a.u.]
δ	distance from the target to the microsphere surface [m]
Δ	relative error of focal length [a.u.]
ε	electric permittivity [F/m]
θ	half angle of the cone of specimen light from objective lens [rad]
λ	wavelength [m]
τ_n	angle function in Mie theory [a.u.]
μ	magnetic permeability [H/m]
π_n	angle function in Mie theory [a.u.]
ψ	scalar function vector spherical harmonic [a.u.]

Subscripts

$\perp$	electric field perpendicular to the incident plane
$//$	electric field parallel to the incident plane
e	even functions
o	odd functions

ABSTRACT

Super-resolution optical microscopes have emerged as powerful and enabling microscopic imaging tools available today. Microsphere-based microscopy is one of the methods which provide the resolution below the diffraction limit.

In this thesis, the analytical separation-of-variables method is used to determine the internal, near and far field distributions of the light fields with microsphere lenses based on Mie theory. The microspheres can focus light and enhance the electromagnetic field along the incidence axis for sub-wavelength illumination. They also enable the collection of near field evanescent diffraction-free lights and transfer them to far field propagating waves. The influence of the refractive index, wavelength and the microsphere size on the location of light focal spot is studied. It has been found that, the distance between focal spot and microsphere center increases with decreasing refractive index contrast, increasing diameter of the microsphere, and decreasing wavelength of the illumination.

The properties of the intensity enhancement capability of photonic nanojets are investigated. The maximum intensity of nanojet is sensitive to the size of microsphere, refractive index, and wavelength. If refractive index contrast is low, the photonic jet can be elongated up to 30 times the wavelength. The dependence of the FWHM on the refractive index, size of microspheres and wavelength of incident light is analyzed.

The virtual imaging plane position and image magnification factor of microspheres are discussed. The characteristics of magnification with different wavelengths, refractive index, and microsphere diameter are analyzed by combination of geometrical optics and Mie theory. The comparison of the focal lengths of microsphere, which is predicted by Mie theory and geometrical optics, is given. The corresponding relative errors are discussed. The images formed by microsphere are mainly affected by radial distortion. This occurs because the magnification of microsphere is different with distance from the optical axis. Several experimental images of microspheres, which produce pincushion distortion, were carried out. A radial distortion model is presented. The distortion of images formed by microsphere are reduced using Matlab applying the model.

DECLARATION

I hereby declare that no portion of the work referred to in the thesis has been submitted in support of an application for another degree or qualification of this or any other university or other institute of learning.

COPYRIGHT STATEMENT

- The author of this thesis (including any appendices and/or schedules to this thesis) owns certain copyright or related rights in it (the “Copyright”) and he has given The University of Manchester certain rights to use such Copyright, including for administrative purposes.

- Copies of this thesis, either in full or in extracts and whether in hard or electronic copy, may be made **only** in accordance with the Copyright, Designs and Patents Act 1988 (as amended) and regulations issued under it or, where appropriate, in accordance with licensing agreements which the University has from time to time. This page must form part of any such copies made.

- The ownership of certain Copyright, patents, designs, trade marks and other intellectual property (the “Intellectual Property”) and any reproductions of copyright works in the thesis, for example graphs and tables (“Reproductions”), which may be described in this thesis, may not be owned by the author and may be owned by third parties. Such Intellectual Property and Reproductions cannot and must not be made available for use without the prior written permission of the owner(s) of the relevant Intellectual Property and/or Reproductions.

- Further information on the conditions under which disclosure, publication and commercialisation of this thesis, the Copyright and any Intellectual Property University IP Policy (see http://documents.manchester.ac.uk/display.aspx?DocID=24420), in any relevant Thesis restriction declarations deposited in the University Library, The University Library’s regulations (see http://www.library.manchest er.ac.uk/about/regulations/) and in The University’s policy on Presentation of Theses

ACKNOWLEDGMENTS

First of all, I am very thankful to my supervisor Professor Lin Li, for his advice and support, for scientific discussions in the Laser Processing Research Centre during my study at The University of Manchester. I am most grateful for his encouragement, without his help, this thesis work would have not been finished.

I would like to thank Dr. Wei Guo for lending his hands whenever I have questions in optical instrumentation. I am grateful to Dr. Sorin Stanescu for helping me prepare experimental samples.

It has been a great pleasure for me to have a chance to work with all the staff and students in the Laser Processing Research Centre (LPRC), at The University of Manchester.

Finally, and most importantly, I am deeply grateful to my parents for their endless love and support all the way through.

CHAPTER 1 Introduction

1.1 Research Motivation

Optical microscopy with high spatial resolving power is indispensable in a wide range of sciences and technologies such as biology, material science and nanotechnologies. There is an enormous growth in the application of optical microscopy for micron and submicron level imaging in recent years.

The wave-like nature of light imposes a seemingly fundamental limit on the resolving power of a microscope. Even without a rigorous description, it is clear that spatial resolution is limited to approximately half the wavelength of light, approximately 200 nm for visible light (400–750 nm). The diffractive limit is always considered as the ultimate barrier for the lens-based optical microscopes to pursue higher resolution. Many researchers have worked on improving this limit and obtained major successes in recent years. The solutions to overcoming this obstacle seem available by using innovative ideas. We have seen exciting developments that achieve improvements in optical resolution. Resolution beyond the diffraction limit is usually obtained by using stimulated emission depletion microscopy(STED), microsphere optical nanoscopy(MONS) near-field scanning optical microscopy (NSOM), total internal reflection fluorescence(TIRF) [1,2,3,4,5,6,7]. Microsphere nanoscopy is a recently developed technology at The University of Manchester. Therefore there is a need to advance the understanding the basic characteristics of microsphere nanoscopy.

1.2 Scientific Challenges

The quality and reproducibility of super-resolution microscopy have been greatly improved in the last few years. Although the diffraction barrier has fundamentally been broken, the drawbacks of present techniques are as evident as their merits. Apart from some specific exceptions such as microsphere microscopy, most other techniques are based on the evanescent field lacking the capability to reflect color information, and are limited to imaging surfaces. The use of the fluorophors is limited to the phenomena originating from nonlinear effects of fluorescence in organic materials, which in turn confines their applications. To activate fluorescence, the incident power of the laser has to be strong that it may result in irreversible damage to the biological sample. The viewing fields of nearly all super-resolution imaging methods are not sufficiently large. Furthermore, how present ideas can be combined to acquire multiple functions will also be a critical part of the process. The use of intensity distribution alone is in complete for rigorous image analysis. More other functional information is always needed.

Comparing to the other super-resolution techniques, the microsphere-based microscopy technique is free from constraints of fluorescence, high intensity, and surface flatness. Even with numerous studies, the mechanisms of high spatial resolution with microsphere-based microscopy are still unclear. Many problems about super-resolution imaging by microspheres still require further investigation. The mechanism of microsphere-based microscopy is explained by the use of geometrical optics approximation, Mie theory, numerical simulation in many literatures [8 , 9 ,10]. The properties of microsphere-based microscopy, such as location of focal points, the imaging plane position and image magnification factor et al., predicted by different methods do not agree among literatures. The characteristics of microsphere interactions with light depended on the refractive index contrast, diameter of the microsphere, and the incident wavelength [10].A reasonable question arises, for example, how large the error of the focal distance between geometrical optics and Mie theory is? How strong is the influence of these parameters on the focal length of the microsphere? What is the relationship between light fields of microsphere and imaging resolution of microscopy?

The images formed by microsphere are mainly affected by radial distortion, similar to a lens. The radial distortion of image causes measurement errors. In order to obtain good image quality, an effective method is needed to eliminate radial distortion and achieve high quality for image of microsphere.

1.3 Aim and Objectives

1.3.1 Aim

The aim of the thesis is to understand the interaction between microspheres and light waves. Mie theory will be used to simulate the relationships between internal field, near field of microsphere and magnification, resolution of microsphere-based microscopy. The properties of microsphere-based microscopy, such as location of focal points, the imaging plane position and image magnification factor will be studied.

1.3.2 Objectives

- To understand the optical properties of microsphere, which would involve both near field and internal field effects by using Mie theory. This will include the investigation of the influence of refractive index contrasts, wavelengths and the microsphere size on the location of focal spot.

- To understand the characteristics of photonic nanojet generated by the microspheres. The dependence of the FWHM on the refractive index, size of microspheres and wavelength of incident light will be analyzed.

- To understand the characteristics of microsphere imaging including image resolution and magnification by combination of geometrical optics and Mie theory. The relative errors of focal length as a function of refractive index contrast, wavelength and microsphere radius will be investigated.

- To understand the radial distortion of microsphere imaging and to develop a radial distortion correction model. Experimental will be carried out to examine various image distortions and pincushion distortion is to be corrected.

1.4 Outline of the Thesis

The thesis is structured as follows:

In Chapter 2, relevant literatures on ordinary optical microscopes and some super-resolution microscopes is the reviewed. The basic characteristics of stimulated emission depletion microscopy, near-field scanning optical microscopy, microsphere-based microscopy are described. The mechanisms of the existing optical microscopes and super-resolution optical microscopes are introduced. Some resolution criterions are reviewed.

In Chapter 3, Mie theory is discussed in detail, and the solutions for internal, near and scattered light fields for a sphere are analyzed. The intensity distributions of light interacting with microspheres are calculated, which depend on the size of the sphere, relative refractive index and the incident wavelength.

In Chapter 4, the super-focusing effects of photonic nanojet are studied. Intensity distributions in the 2D and 3D photonic nanojets are simulated. The influence of the wavelength, refractive index contrast and microsphere diameter on focal point are investigated. The properties of full-width half-maximum of photonic nanojet, which corresponds to the limit of resolution of Houston’s criterion, are discussed.

In Chapter 5, the properties of image magnification for microspheres with different refractive index contrasts, wavelengths and radius are given. The focal spots position of microsphere predicted by Mie theory, are compared with those predicted by geometrical optics (GO), the corresponding relative errors are discussed.

In Chapter 6, in a similar manner as Chapter 3 and 4, the characteristics of sample microspheres in Wang’s and Darafsheh’s experiments are analyzed respectively. The resolution and magnification of the images for the spheres are investigated. A comparison in the image magnification for different sphere diameters between that calculated with geometrical optics and Wang’s approximations is given, the valid range of two methods is further investigated.

In Chapter 7, the distortion aberration of image is analyzed both experimentally and theoretically. A radial distortion model was established to describe the phenomenon and correction was attempted using the model and Matlab image processing tools.

CHAPTER 2: Literature Review

2.1 Basic Principles of the Optical Microscope

2.1.1 The optical components of microscope

Around the beginning of the 1600's, through work attributed to the Janssen brothers in the Netherlands and Galileo in Italy, a compound microscope was invented. The optical microscope is an optical instrument to produce a magnified image of an object. It is projected onto the retina of the eye or onto an imaging device， as shown in Figure 2. 1 . The basic optical components of an optical microscope include two lenses, the objective lens and the eyepiece (ocular), to produce the final magnification of the image. The objective lens collects light diffracted by the objects and forms a magnified real image at the real intermediate image plane near the eyepieces. Then the intermediate image is examined by the eyepiece and eye, which together form a real image on the retina. Both the objective and condenser contain multiple lens elements that perform close to their theoretical diffraction limits. The optical components of a modern microscope are very complex. The optical path has to be very accurately set up and controlled.

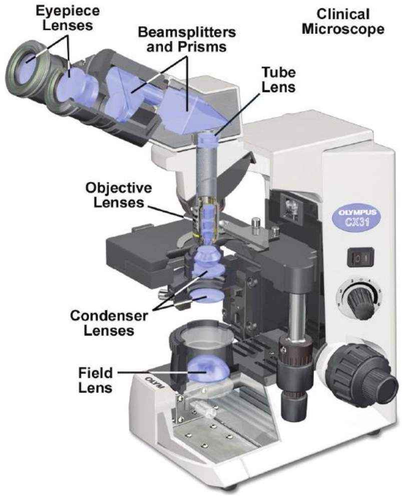

Figure 2. 1 The compound light microscope [7].

The action of lenses on light are revealed by ray tracing and explained by principles of refraction and reflection. Microscope objectives contain multiple lens elements. When a microscope objective lens focuses light on a specimen, the image is both real and magnified.

Modern microscopes with infinity focus objective lenses follow the same optical principles described above for generating a magnified real image. Only the optical design is somewhat different. For an objective lens with an infinity focus design, the specimen is located at the focus of the lens, and parallel bundles of rays emerging from the back aperture of the lens are focused to infinity and do not form an image; it is the job of the tube lens in the microscope body to receive the rays and form a real intermediate image at the eyepiece. The advantage of this design is that it allows greater flexibility for microscope design while preserving the image contrast and resolution provided by the objective.

2.1.2 Resolution criteria and resolution limit

The image of a self-luminous point object in a microscope or any other image-generating instrument is a diffraction pattern created by the action of interference in the image plane [11]. The cross sectional intensity profile of the diffraction pattern is called the objects' Point Spread Function (PSF), and the two-dimensional PSF of an optical microscope is known as the "Airy disk". The central diffraction of an Airy disk contains 84% of the light from the point source [12,13,14].

For a microscope objective lens, the aperture angle is described by the numerical aperture (NA), which is defined by

$$NA = m \sin\theta \tag{2. 1}$$

where m is the refractive index of the medium between the lens and the specimen, and θ is the half angle of the cone of specimen light accepted by the objective lens.

The far-field spatial resolution of an optical instrument is mainly limited by the diffraction of light. Two-point resolution is defined as the system's ability to resolve two point sources of equal intensity. There are several diffraction-related resolution criteria, such as Rayleigh [15], Abbe [16], Sparrow [17], and Houston [18], which can determine how close two sources can be discerned in the image plane.

Rayleigh's criterion [15] is defined that two point sources are resolved when the maximum of the diffraction pattern of one falls on the minimum of the pattern of the other:

$$d = \frac{0.61\lambda}{NA} \tag{2. 2}$$

where d is the distance of two point sources, λ is the wavelength of the illumination. If the distance between two point sources is greater than this value, the two point sources are considered to be resolved. Note that the Rayleigh criterion is based upon assumption that the two point sources are incoherent.

In the Abbe's microscope theory [16], incident light is diffracted by object features, which are considered as a diffraction grating with period d. The diffracted orders can be collected totally or partially by the imaging system. The Abbe diffraction limit is defined:

$$d = \frac{0.5\lambda}{NA} \tag{2. 3}$$

The Abbe limit is ~200-250nm for conventional white light microscopy systems.

According to the Sparrow criterion [17], two point sources are resolved if the second-order derivative of the composite intensity distribution at the center of the diffraction image just vanishes. In this case, the composite intensity distribution shows no saddle at the middle because both central maxima and the minimum in between just coincide [17]:

$$d = \frac{0.473\lambda}{NA} \tag{2. 4}$$

Houston criterion[18] is that the two point sources are just resolved if the distance d between the central maxima of the composite intensity distribution equals the full width at half-maximum of the diffraction pattern of either point source [18]:

$$d = FWHM = \frac{0.515\lambda}{NA} \tag{2. 5}$$

2.2 Super-resolution Microscopy and Theoretical Limitations

2.2.1 Stimulated emission depletion microscopy

For more than a century, many efforts have been taken to break the diffraction limit in microscopy [19,20]. Super-resolution microscopy allows the capture of images with a higher resolution than the diffraction limit [1, 21, 22, 23].

Stenfan W. Hell and Jan Wichmann developed Stimulated emission depletion (STED) microscopy in 1994 [1], and was first experimentally demonstrated by Hell and Thomas Klar in 1999 [21]. Hell was awarded the Nobel Prize in Chemistry in 2014 for its development. STED is a process that provides super resolution imaging by selectively deactivating fluorophores. The principle of this approach is shown in Figure 2. 2. Molecules in the fluorescent state S_1 return to the ground state S_0 by spontaneous fluorescence emission. Return to S_0 might also be optically enforced through stimulated emission. To prevail over the spontaneous emission, stimulated emission depletion of the S_1 requires relatively intense light pulses with durations of a fraction of the S_1 lifetime. STED microscopy operates as follows: in the first step of the acquisition, the sample molecules in the diffraction-limited spot are excited by a normal mode (Airy disk) laser pulse with duration of picoseconds or less. This is followed immediately (within a few hundred picoseconds) by a second donut-mode laser pulse irradiating the same region, which induces stimulated emission in the majority of the dye molecules, except those at the center of the focus (due to the intensity distribution of the donut mode), as shown in Figure 2.3.The sample molecules that are still in the excited state, and then left to fluoresce normally, which is detected. Because of the depletion, however, the fluorescence collection is effectively confined to a spot with sub-diffraction dimensions, leading to an increased resolution.

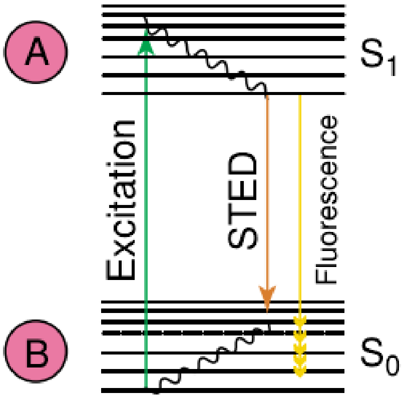

Figure 2. 2 STED principle [22]

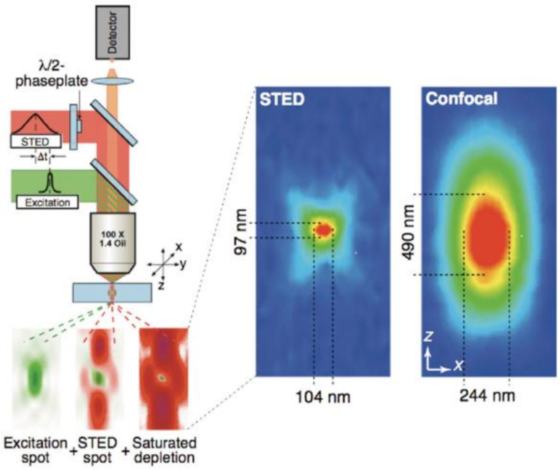

Figure 2. 3 STED microscopy [22]

This measurement cycle is then repeated at the next point on the sample, until a complete image is obtained. In this way, a spatial resolution down to a few tens of nanometers has been reported [23,24,25,26,27,28]. The most attractive features of donut-based microscopy are that the effective resolution increase is completely dictated by the experimental setup and the irradiation powers used. Moreover, the imaging is altered directly, and obtaining a sub-diffraction resolution would require additional software processing and standard microscope objective lens are still operating within the diffraction limit. In addition, if stimulated emission is used, then the image acquisition times can be as fast as any laser-scanning microscope. Saturation of fluorescent particles by the powerful laser beam is another problem. In addition, the technique cannot be applied to metals, ceramics and semiconductors where labeling of protein by fluorescent particles is not possible.

2.2.2 Near-field scanning optical microscopy (NSOM)

STED microscopy can obtain super-resolution in far-field optics. Near Field Scanning Optical Microscopy (NSOM) works in the optical near field zone where the evanescent waves, linked to sub-wavelength optical component to target distances, are predominant. Access to the evanescent waves allows achieving high optical resolution, which resolution < 100 nm. The development of NSOM may be summarized through the different historical steps shown in Table 1. When a small object is illuminated, its fine structures with high spatial frequency generate a localized field that decays exponentially normal to the object. This evanescent field on the tiny substructure can be used as a local source of light illuminating and scanning a sample surface so close that the light interacts with the sample without diffracting. There are two methods by which a localized optical field suitable for NSOM can be generated.

Table 1 Development of NSOM

1928	Synges idea[29]
1972	Ash & Nicholls' First demo in microwaves[30]
1984	Lewis & Pohl: First version of NSOM[31]
1986	Reddick & Warmack & Ferrell: First PSTM[32]
1986	Courjon: First STOM
1990	Feedback progress
1990	Photonic or plasmonic applications
1990	Fluorescence applications
1993	Betzig: Single molecule detection with NSOM[33]
1994	Novotny & Pohl: Near field modeling[34]
1993-1995	Kawatan &Wickramasinghe: "Apertureless"
1998	Veerman&van Hulst: Defined aperture probes[35]
1999	Dunn: near field and biology &Combined techniques with NSOM[36]
2002	Frey: Tip-on-aperture configuration[37]
now	Enhanced NSOM & Bio/chem and NSOM & Combined techniques with NSOM[38]

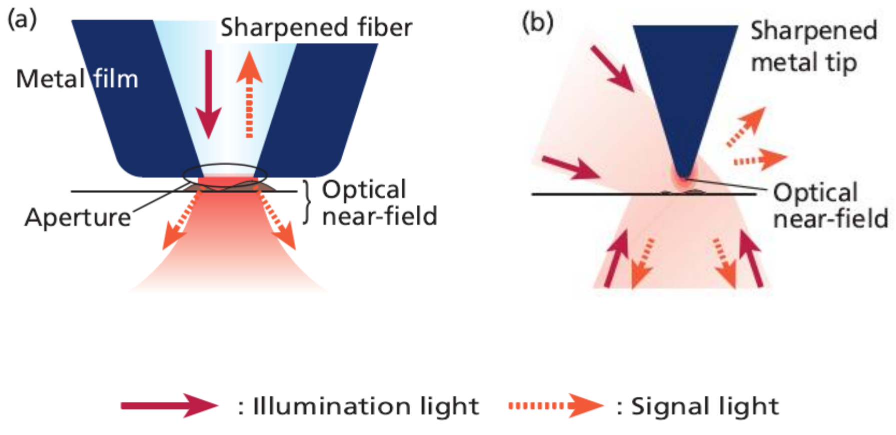

Figure 2. 4 (a) Schematic of aperture NSOM; (b) Schematic of apertureless (scattering) NSOM [39].

As illustrated in Figure 2. 4, one method uses a small aperture at the apex of a tapered optical fiber coated with metal. Light sent down the fiber probe and through the aperture illuminates a small area on the sample surface. The fundamental spatial resolution of aperture NSOM is determined by the diameter of the aperture, which ranges from 10 to 100 nm. In the other method, called apertureless (or scattering) NSOM and illustrated in Figure 2. 4(b), a strongly confined optical field is created by external illumination at the apex of sharpened metal or dielectric tip. Spatial resolution approaching the atomic scale is expected, and laboratory experiments have yielded resolutions ranging from 1 to 20 nm. A rather large (diffraction limited) laser spot focused on a tip apex frequently causes an intense background that reduces the signal-to-noise ratio.

The simplest setup for aperture NSOM, a configuration with local illumination and local collection of light through an aperture, is illustrated in Figure 2. 5. The probe quality and the regulation system for tip-sample feedback are critical to NSOM performance. The light emitted by the aperture interacts with the sample locally. It can be absorbed, scattered, or phase-shifted, or it can excite fluorescence. The fabrication of fiber-based optical probes can be divided into the three main steps: (a) the creation of a taper structure with a sharp apex, (b) coating with a metal (Al, Au, Ag) to obtain an entirely opaque film on the probe, and (c) the formation of a small aperture at the apex.

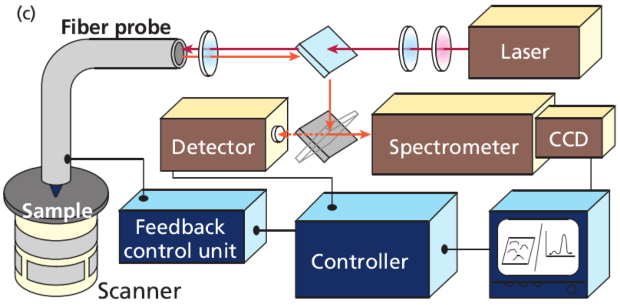

Figure 2. 5 Schematic of standard NSOM setup with a local Illumination and local collection configuration [39].

There are two methods used to make tapered optical fibers with a sharp tip and reasonable cone angle. One is the heating-and-pulling method, where the fiber is locally heated using a CO_2 laser and is subsequently pulled apart. The other method, based on chemical etching in a hydrofluoric acid (HF) solution, is more reproducible production and can be used to make many probes at the same time [40,41,42].

2.3 Microsphere Optical Nanoscopy

Li and his team developed an approach for microsphere optical nanoscopy by placing a transparent microsphere on the surface of the sample, a resolution of about 50 nm was achieved [3]. This technique uses a dielectric microsphere as a “magnifying lens” creating a virtual image of an object located at the surface of the structure. Visualization of the virtual images of the surface requires a change of the depth of focusing. In 2013, Li presented direct white-light optical imaging of 75-

nm adenoviruses by submerged microsphere optical nanoscopy (SMON) without the use of fluorescent labeling or staining [2]. This significant progress undoubtedly will bring out a profound impact on related disciplines in biology, chemistry, medicine, and semiconductor industry. By combining a microsphere with a confocal optical microscope, 25nm resolution was demonstrated by Li’s team.

2.3.1 Experiments on microsphere optical nanoscopy

In the experiments, the microspheres were placed on the top of the object surface by self-assembly, as shown in Figure 2. 6. The diameter of microsphere was $4.74\mu m$. A halogen lamp with a peak wavelength of 600 nm was used as the white-light illumination source. The objects were gratings, which consisted of 360nm-wide lines, spaced 130 nm apart. The lines gratings cannot be directly resolved by the optical microscope without particles on top because of the diffraction limit. Only those lines with microspheres on top of them have been resolved. The microsphere superlenses collect the underlying near field object information and magnify it. The microsphere nanoscope resolves the tiny pores that are well beyond the diffraction limit, giving a resolution of between $\lambda / 8$ ($\lambda = 400$ nm) and $\lambda / 14$ ($\lambda = 750$ nm) in the visible spectrum range. The performance of microsphere superlens is affected by the near-field interaction of the sphere and the substrate. The optical microsphere nanoscope can be used in both the reflection and transmission modes.

Li et al also reported another microsphere optical nanoscopy (SMON) by the using submerged microspheres [2]. Optically transparent microspheres with a diameter of 100 mm, were placed over the specimen and deposited in deionized water, as shown in Figure 2.7. The sub-diffraction-limited objects were a Blu-Ray DVD disk with approximately 100-nm line spacing. The microspheres of $\mathrm{Ba}TiO_3$ (diameter $100\mu m$) submerged in water under white light (reflective mode) illumination.

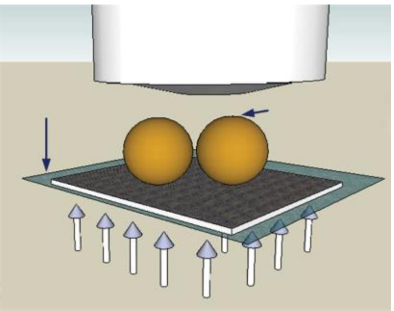

Figure 2. 6 Schematic of a transmission mode microsphere nanoscope [3].

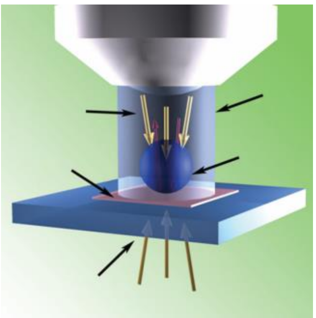

Figure 2.7 Submerged microsphere optical nanoscopy [2]

Both the reflection and transmission modes were used in the optical microscope. The structure (100-nm spacing) observed by the submerged microsphere optical nanoscopy technique is well beyond the spatial resolution limit of standard optical microscopes. The imaging result is shown in Figure 2.8.

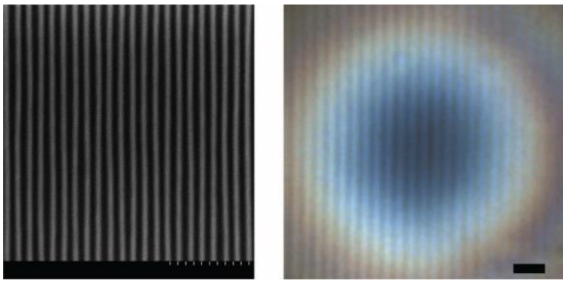

Figure 2.8 Imaging of a Blu-Ray DVD disk by (a) scanning electron microscopy; (b) submerged microsphere optical nanoscopy [3].

There are also many reported investigations to study microsphere microscopy [2,4,43,44,45,46,47,48,49,50,51]. Xiang Hao et al experimentally demonstrated that the microspheres can discern the details of the object whose size are below the conventional diffractive limit and such capability can be reinforced if semi-immersing the corresponding microspheres in liquid meniscus [45].

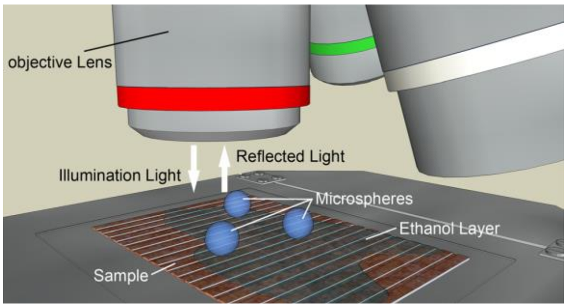

Figure 2. 9 X. Hao's microsphere-based nanoscope [43].

The experiment is shown in Figure 2. 9. The different images of the surface of the blue-ray disk were given in Figure 2. 10, which generated by scanning electron microscope, optical microscope, 3μm microsphere and 3μm microsphere semi-immersed in the ethanol droplet, respectively.

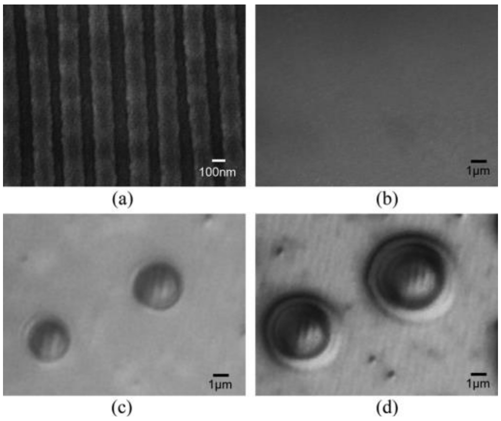

Figure 2. 10 The images of the surface of the blue-ray disk generated by different technical methods: (a) scanning electron microscope; (b) optical microscope with 100 ×objective lens; (c) 3 μm microsphere; (d) 3μm microsphere semi-immersed in the ethanol droplet[45].

Darafsheh experimentally demonstrated the feasibility of performing optical microscopy with spatial resolution $\lambda/4$ using high-index microspheres embedded in transparent elastomers [46].

2.3.2 The imaging mechanism of the microsphere nanoscope

Many researchers investigate mechanism of microsphere and try to provide physical insight for this super-resolution phenomenon [2, 3,43,49,52,53,54]. By using the microspheres, optical resolution has been demonstrated in the range of 50–120 nm. This resolution is clearly beyond the optical diffraction limits of these microscopes. The imaging resolution and magnification of the microsphere superlenses are fundamentally related to their focus properties. The microspheres can generate photonic jets simulated using Mie theory [3,55,56,57]. The calculated super-resolution window for different refractive indexes of the sphere and the size parameters for spheres immersed in air are shown in Figure 2. 11. It can be seen that refractive index has a strong effect on super-resolution. The practical size window for $n=1.46$ microspheres is recommended as 2 μm < diameter < 9 μm for 50-nm-resolution. The super-resolution strength is mainly dependent on a narrow window of the refractive index of the sphere and the size parameters [3].

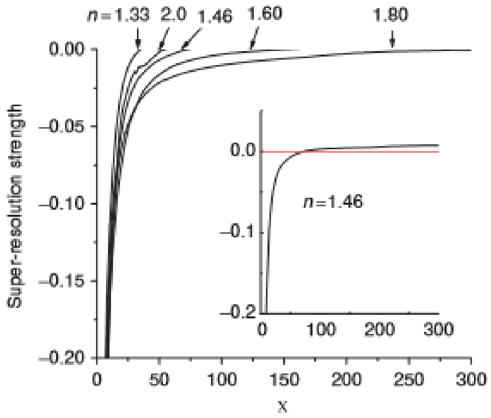

Figure 2. 11 Super-resolution strength, defined as (size of focus spot - Rayleigh limit)/R, as a function of size parameter x, defined as x=2πR/λ, for different refractive index particles [3].

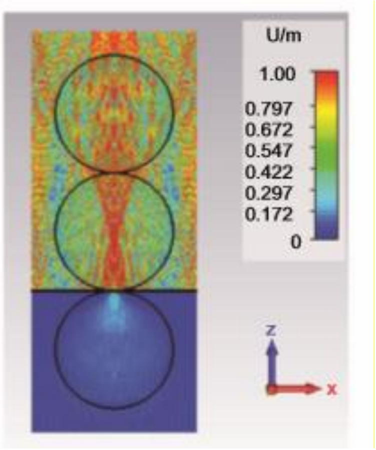

Figure 2. 12. The conjugate model for microsphere converts the evanescent waves from the target surface into propagating waves [2].

The process of light propagation is simulated by using electromagnetic numerical method. When a microsphere is submerged in the water, a weak energy coupling caused by the conversion of the evanescent waves to propagating waves occurs through total internal reflection.

The converted propagating waves contain the high spatial-frequency information of the sub-wavelength slits.

When the transmitted light passes into the microsphere, the light is focused, and the photonic nanojets are generated. The photonic jets arrive on the object surface and illuminate the area below the microsphere at a high intensity and a high resolution, beyond the diffraction limit. The microsphere re-collects the light scattered by the objects and converts the high spatial frequency evanescent waves (no diffraction limits) into propagating waves that can be collected by far-field imaging, which is illustrated in Figure 2. 12.

The evanescent waves in the near field are converted into the magnified prorogating waves in the far field by the microsphere through the total internal reflection. Because evanescent waves do not have a diffraction limit, the transformation of the evanescent wave magnifies propagating wave within the optical resolution limit of a standard optical microscope.

Duan, et al studied the direct imaging calculation with classical imaging theory [52]. They theoretically model the imaging process through a microlens with vectorial electromagnetic analysis, and then exclude the previously plausible explanation of super-resolution based on the superfocusing effect. Using the generalized multisphere Mie theory, A. Heifetz et al theoretically investigated backscattering from a bi-sphere system in a water background medium [53]. They found that the nanosphere can be located with a subdiffraction transverse spatial resolution in the H−direction as fine as $\lambda_{water}/3$ for the resonant case when the nanosphere is approximately $\lambda_{water}/4$ behind the microsphere.

2.4 Summary

The desire that drives the development of optical super-resolution microscopy is that visualizing samples with such unprecedented resolution will yield miraculous discoveries. The applications of these methods have already begun, but the full realization of the initial dream is yet to come. The researchers have long been eager to image fine details below the surface. The universal and economical method to obtain sub-10-nm optical resolution would come true in the near future.

The above studies covered only a small portion of the research currently being pursued in the area of super-resolution optical microscopes, involving stimulated emission depletion microscopy, near-field scanning optical microscopy, microsphere-based microscopy. The mechanisms of those super-resolution microscopes are described. The principles in super-resolution imaging are analyzed. Micro-optical systems by microspheres and their characteristics are introduced. The super-resolution microscopy has proved valuable for the study of area of molecules and nanometer-size objects.

CHAPTER 3: Analyzing Electromagnetic Field of Microsphere Using Mie Theory

3.1 Mie Theory

The physics of the interaction of electromagnetic wave with particles is complicated. Interaction between particles with light wave is analyzed based on Maxwell equations. Gustav Mie derived the solution for an isotropic homogeneous sphere by using the separation of variables technique in 1908 [58]. Mie theory is a complete formal solution to Maxwell's electromagnetic equations, and can be used to describe the internal field, near field and far field and has no size limitations and converges to the limit of geometric optics for sphere [59,60,61].

In the following discussion, suppose that a plane x-polarized wave with amplitude E_0 propagates along z axis. Electromagnetic field in isotropic, homogeneous medium must satisfy the Maxwell wave equation [62,63,64]:

$$\nabla^2\vec{E}+k^2\vec{E}=0 \qquad (3.\ 1)$$

$$\nabla^2\vec{H}+k^2\vec{H}=0 \tag{3. 2}$$

where $k^2=\omega^2\varepsilon\mu$ is wave vector in the surrounding medium, ε and μ are permittivity and permeability in the surrounding medium respectively.

The relation between $\vec{E}$ and $\vec{H}$ is [65,66]

$$\vec{E}=\frac{i\omega\mu}{k^2}\nabla\times\vec{H} \tag{3. 3}$$

$$\vec{H}=\frac{1}{i\omega\mu}\nabla\times\vec{E} \tag{3. 4}$$

Defining a scalar function ψ, ψ is a solution to the scalar wave equation:

$$\nabla^2\psi+k^2\psi=0 \tag{3. 5}$$

Then, three independent vector solutions can be constructed:

$$\vec{M}=\nabla\times(\vec{r}\,\psi) \tag{3. 6}$$

$$\vec{L}=\nabla\psi \tag{3. 7}$$

$$\vec{N}=k^{-1}\cdot\nabla\times\vec{M} \tag{3. 8}$$

where $\vec{r}$ is the radius vector, then $\vec{M}$, $\vec{N}$ and $\vec{L}$ are solutions to the vector wave equation in spherical coordinates. $\vec{M}$ and the associated $\vec{N}$ will be taken as solutions to the field equations.

In spherical coordinates (r,θ,φ), the scalar wave equation can be expressed by [64]

$$\frac{1}{r^2}\frac{\partial}{\partial r}(r^2\frac{\partial\psi}{\partial r})+\frac{1}{r^2\sin\theta}\frac{\partial}{\partial\theta}(\sin\theta\frac{\partial\psi}{\partial\theta})+\frac{1}{r^2\sin^2\theta}\frac{\partial^2\psi}{\partial\varphi^2}+k^2\psi=0 \qquad (3.\ 9)$$

By using a separation of variables, the scalar solution ψ_{emn} ,ψ_{omn} are obtained satisfy the scalar wave equation in spherical coordinates [64]

$$\psi_{emn}=\cos(m\varphi)P_n^m(\cos\theta)z_n(kr) \qquad (3.\ 10)$$

$$\psi_{omn}=\sin(m\varphi)P_n^m(\cos\theta)z_n(kr) \qquad (3.\ 11)$$

where $z_n(kr)$ is any of the four spherical Bessel functions, either spherical Bessel functions $j_n(kr)$, or spherical Neumann functions $y_n(kr)$, or spherical Hankel functions of the first kind $h_n^{(1)}(kr)$, or of the second kind $h_n^{(2)}(kr)$. $P_n^m(\cos\theta)$ is Legendre functions of the first kind of degree n ($n=1,2,...$) and order m ($m=0,\pm1,\pm2,...\pm n$). The subscripts e and o denote even and odd functions, respectively.

The vector spherical harmonics are generated by ψ_{emn} ,ψ_{omn} ,which is a set of linear independent and orthogonal vector:

$$\vec{M}_{emn}=\nabla\times(\vec{r}\psi_{emn}) \qquad \vec{M}_{omn}=\nabla\times(\vec{r}\psi_{omn}) \qquad (3.\ 12)$$

$$\vec{N}_{emn} = k^{-1} \cdot \nabla \times \vec{M}_{emn} \qquad \vec{N}_{omn} = k^{-1} \cdot \nabla \times \vec{M}_{omn} \tag{3. 13}$$

The explicit expressions in component form are [64]

$$\vec{M}_{enm}(kr,\theta,\varphi) = \frac{-m}{\sin\theta} \sin m\phi P_n^m(\cos\theta) z_n(kr)\vec{e}_\theta - \cos m\phi \frac{dP_n^m(\cos\theta)}{d\theta} z_n(kr)\vec{e}_\varphi \tag{3. 14}$$

$$\vec{M}_{onm}(kr,\theta,\varphi) = \frac{m}{\sin\theta} \cos m\phi P_n^m(\cos\theta) z_n(kr)\vec{e}_\theta - \sin m\phi \frac{dP_n^m(\cos\theta)}{d\theta} z_n(kr)\vec{e}_\varphi \tag{3. 15}$$

$$\begin{aligned} \vec{N}_{enm}(kr,\theta,\varphi) = {} & \frac{n(n+1)}{kr} \cos m\phi z_n(kr) P_n^m(\cos\theta)\vec{e}_r \\ & + \mathrm{cosm}\,\phi \frac{1}{kr} \frac{d[rz_n(kr)]}{dr} \cdot \frac{dP_n^m(\cos\theta)}{d\theta} \vec{e}_\theta \\ & - m \sin m\phi \frac{1}{kr} \frac{d[rz_n(kr)]}{dr} \frac{P_n^m(\cos\theta)}{\sin\theta} \vec{e}_\varphi \end{aligned} \tag{3. 16}$$

$$\begin{aligned} \vec{N}_{onm}(kr,\theta,\varphi) = {} & \frac{n(n+1)}{kr} \sin m\phi z_n(kr) P_n^m(\cos\theta)\vec{e}_r \\ & + \sin m\phi \frac{1}{kr} \frac{d[rz_n(kr)]}{dr} \cdot \frac{dP_n^m(\cos\theta)}{d\theta} \vec{e}_\theta \\ & + m \cos m\phi \frac{1}{kr} \frac{d[rz_n(kr)]}{dr} \frac{P_n^m(\cos\theta)}{\sin\theta} \vec{e}_\varphi \end{aligned} \tag{3. 17}$$

Any solution to the field equations can be expanded in an infinite series of the functions (3.14)-(3.17). Thus, by using vector harmonics，the problem of scattering by an arbitrary sphere can be solved.

3.2 Electromagnetic Field of Single Sphere

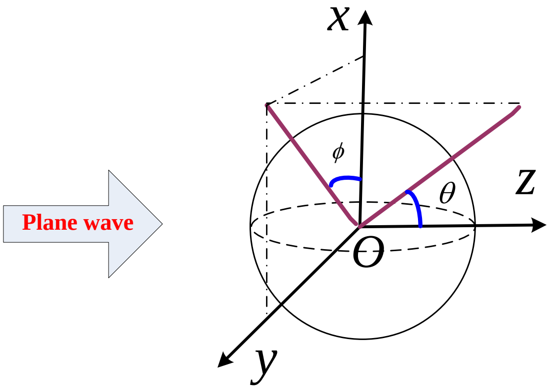

Figure 3. 1 Plane wave incident on a single sphere

Let us consider an incident plane wave propagating in the direction of the positive z axis with x polarized. The sphere is illuminated by an incident plane wave with wavelength λ, as shown in Figure 3. 1.

The incident, internal and scattered fields are expanded in vector spherical harmonics [64]:

Incident field:

$$\vec{E}_i = E_0 \sum_{n=1}^{\infty} i^n \frac{2n+1}{n(n+1)} \left[\vec{M}^{(1)}_{o1n}(r,\theta,\varphi) - i\vec{N}^{(1)}_{e1n}(r,\theta,\varphi) \right] \tag{3. 18}$$

$$\vec{H}_i = \frac{-k}{\omega\mu} E_0 \sum_{n=1}^{\infty} i^n \frac{2n+1}{n(n+1)} \left[\vec{M}^{(1)}_{e1n}(r,\theta,\varphi) + i\vec{N}^{(1)}_{o1n}(r,\theta,\varphi) \right] \tag{3. 19}$$

Internal field:

$$\vec{E}_1 = E_0 \sum_{n=1}^{\infty} i^n \frac{2n+1}{n(n+1)} \left[c_n \vec{M}_{o1n}^{(1)}(r,\theta,\varphi) - i d_n \vec{N}_{e1n}^{(1)}(r,\theta,\varphi) \right] \tag{3. 20}$$

$$\vec{H}_1 = \frac{-k_1}{\omega\mu_1} E_0 \sum_{n=1}^{\infty} i^n \frac{2n+1}{n(n+1)} \left[d_n \vec{M}_{e1n}^{(1)}(r,\theta,\varphi) + i c_n \vec{N}_{o1n}^{(1)}(r,\theta,\varphi) \right] \tag{3. 21}$$

Scattered field:

$$\vec{E}_s = E_0 \sum_{n=1}^{\infty} i^n \frac{2n+1}{n(n+1)} \left[-b_n \vec{M}_{o1n}^{(3)}(r,\theta,\varphi) + i a_n \vec{N}_{e1n}^{(3)}(r,\theta,\varphi) \right] \tag{3. 22}$$

$$\vec{H}_s = \frac{-k}{\omega\mu} E_0 \sum_{n=1}^{\infty} i^n \frac{2n+1}{n(n+1)} \left[a_n \vec{M}_{e1n}^{(3)}(r,\theta,\varphi) + i b_n \vec{N}_{o1n}^{(3)}(r,\theta,\varphi) \right] \tag{3. 23}$$

where E_0 is the amplitude of the electric field at $z=0$, μ_1 is the permeability of the sphere. k_1 is the wave number in the sphere. The a_n, b_n, c_n and d_n are the expansion coefficients of the scattered and internal field. In Eq. (3.18) –Eq. (3.23), the superscript (1) of the vector harmonics denotes $j_n(kr)$ to the kind spherical Bessel functions $z_n(kr)$, and the superscript (3) denotes $h_n^{(1)}(kr)$.

The continuity of the tangential components of fields on the surface of the sphere makes it possible to find the analytical formulas of the expansion coefficients of the internal and scattered field. The Maxwell's boundary conditions are applied at the surface of sphere [64]:

$$\left.\begin{array}{ll} E_{i\theta}+E_{s\theta}=E_{1\theta} & E_{i\phi}+E_{s\phi}=E_{1\phi} \\ H_{i\theta}+H_{s\theta}=H_{1\theta} & H_{i\phi}+H_{s\phi}=H_{1\phi} \end{array}\right\} \quad \text{at } r=a \tag{3. 24}$$

The boundary conditions can be resolved to obtain all unknown expansion coefficients a_n b_n c_n and d_n [64,67]：

$$a_n=\frac{\mu m^2 j_n(mx)[xj_n(x)]'-\mu_1 j_n(x)[mxj_n(mx)]'}{\mu m^2 j_n(mx)[xh_n^{(1)}(x)]'-\mu_1 h_n^{(1)}(x)[mxj_n(mx)]'} \tag{3. 25}$$

$$b_n=\frac{\mu_1 j_n(mx)[xj_n(x)]'-\mu j_n(x)[mxj_n(mx)]'}{\mu_1 j_n(mx)[xh_n^{(1)}(x)]'-\mu h_n^{(1)}(x)[mxj_n(mx)]'} \tag{3. 26}$$

$$c_n=\frac{\mu_1 j_n(x)[xh_n^{(1)}(x)]'-\mu_1 h_n^{(1)}(x)[xj_n(x)]'}{\mu_1 j_n(mx)[xh_n^{(1)}(x)]'-\mu h_n^{(1)}(x)[mxj_n(mx)]'} \tag{3. 27}$$

$$d_n=\frac{\mu_1 mj_n(x)[xh_n^{(1)}(x)]'-\mu_1 mh_n^{(1)}(x)[xj_n(x)]'}{\mu m^2 j_n(mx)[xh_n^{(1)}(x)]'-\mu_1 h_n^{(1)}(x)[mxj_n(mx)]'} \tag{3. 28}$$

The prime denotes derivation with respect to the argument. x is the size parameter, and m is the relative refractive of particle and medium. Thus， all fields of sphere are determined [64,68].

3.3 Numerical Results for Far Field of Single Sphere

Considering the far field at large distances, the far electric field can be given as follows [69,70,71,72,73]:

$$E_{s\theta} = E_0 \frac{i\exp(ikr)}{kr} S_2(\theta)\cos\phi \qquad (3.\ 29)$$

$$E_{s\phi} = -E_0 \frac{i\exp(ikr)}{kr} S_1(\theta)\sin\phi \qquad (3.\ 30)$$

where

$$S_1(\theta) = \sum_{n=1}^{\infty} \frac{(2n+1)}{n(n+1)}[a_n\pi_n(\cos\theta) + b_n\tau_n(\cos\theta)] \qquad (3.\ 31)$$

$$S_2(\theta) = \sum_{n=1}^{\infty} \frac{(2n+1)}{n(n+1)}[a_n\tau_n(\cos\theta) + b_n\pi_n(\cos\theta)] \qquad (3.\ 32)$$

π_n, τ_n are the angle dependent function,

$$\pi_n = \frac{P_n^1}{\sin\theta}, \quad \tau_n = \frac{dP_n^1}{d\theta} \qquad (3.\ 33)$$

and can be computed by upward recurrence from the relations

$$\pi_n = \frac{2n+1}{n-1}\pi_{n-1}\cos\theta - \frac{n}{n-1}\pi_{n-2} \qquad (3.\ 34)$$

$$\tau_n = n\pi_n\cos\theta - (n+1)\pi_{n-1} \qquad (3.\ 35)$$

If the incident light I_i is polarized parallel to a particular scattering plane, the scattered light is also polarized parallel to the scattering plane. The intensity of scattered light for the incident light polarized parallel to the scattering plane:

$$I_{//} = |S_2|^2 I_i \tag{3. 36}$$

If the incident light is polarized perpendicular to the scattering plane, the intensity of the scattered light is

$$I_{\perp} = |S_1|^2 I_i \tag{3. 37}$$

If the incident light is unpolarized， the intensity of the scattered light is

$$I_s = \frac{1}{2}(|S_2|^2 + |S_1|^2) I_i \tag{3. 38}$$

A microsphere with a size parameter $x = 3$ ($x = 2\pi R/\lambda$), and refractive index $m = 1.33 + i \times 10^{-8}$ is computed. The wavelength of incident wave is 0.55μm. The far field intensity of microsphere is show in Figure 3. 2 (a). The result was verified by comparing to that of Figure 4.9 in Ref [64]. They agree with very well.

Having validated the procedure, the far field of microsphere is studied in detail. A SiO_2 microsphere with radius $R = 2.37\mu m$ and refractive index $m = 1.46$ is illuminated by unpolarized plane wave with wavelength $\lambda = 0.6\mu m$. The intensity is plotted as a function of scattering, shown in Figure 3. 3. The scattered intensity in the forward direction is more than 600 times greater than that in the backward direction.

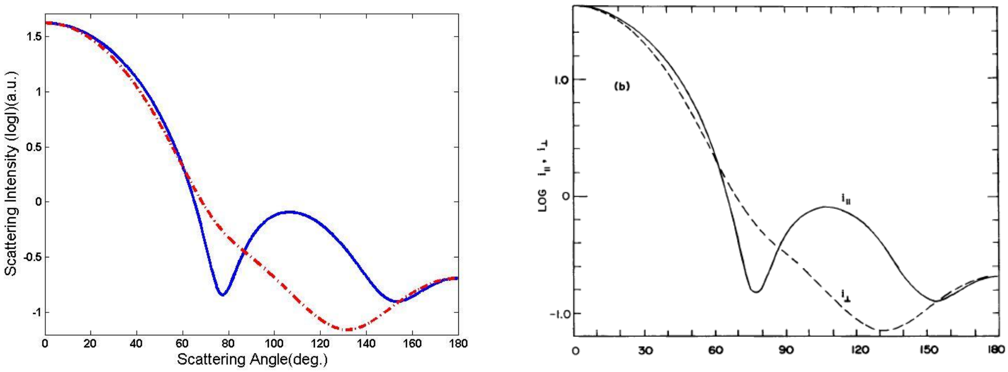

(a) **(b)**

Figure 3. 2 The scattering intensity of sphere with $x = 3$ and $m = 1.33 + i \times 10^{-8}$ illuminated by plane wave $\lambda = 0.55\mu m$. (a) Blue curve is the incident light polarized perpendicular to the scattering plane, and red curve is incident light polarized parallel to a particular scattering; (b) result with same parameter in ref[64]

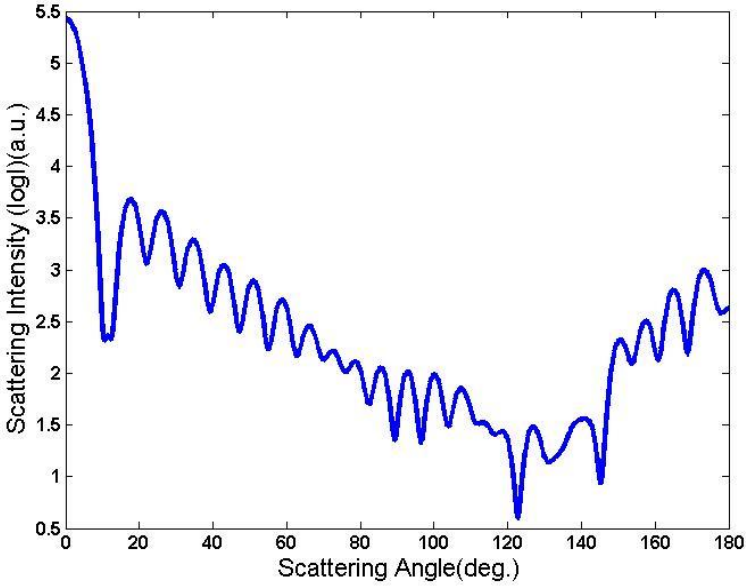

Figure 3. 3 the scattering intensity distribution for a SiO_2 microsphere with radius $R = 2.37\mu m$ and refractive index $m = 1.46$ illuminated by unpolarized plane wave $\lambda = 0.6\mu m$.

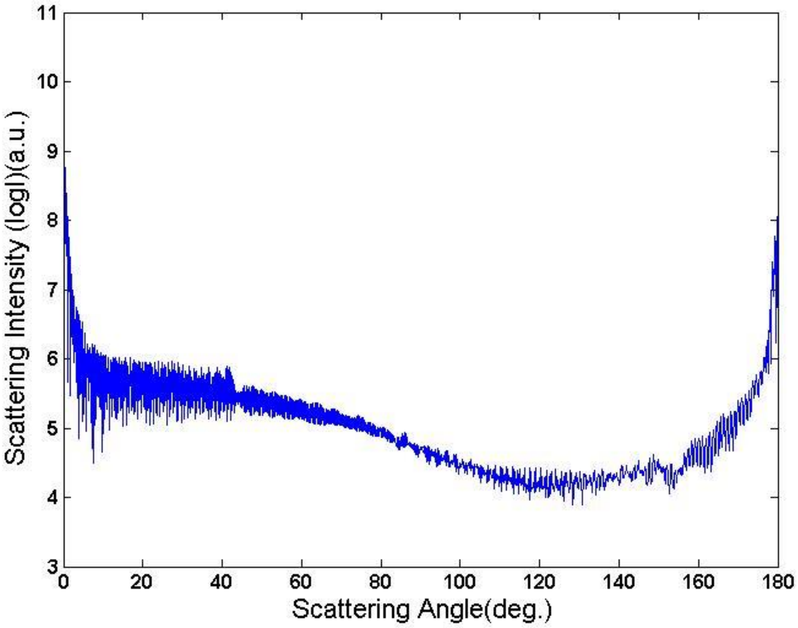

Figure 3. 4 The scattering intensity distribution with scattering angle for a large $BaTiO_3$ microspheres with $R = 50\mu m$, $m = 1.9$ and $\lambda = 0.6\mu m$

In Figure 3. 4, the scattering intensity distributions are calculated with a scattering angle for a large $BaTiO_3$ microspheres with $R = 50\mu m$, $m = 1.9$ and $\lambda = 0.6\mu m$. The scattering intensity diminishes as scattering angle increases for each particle. At small angles, the scattering intensity is stronger for large particles than that from small particles at the same scattering angle.

3.4 Numerical Results for Internal and Near Fields of a Single Sphere

According to discussions in Section 3.2, by substitution of expansion coefficients in Eq.(3.25)-Eq.(3.28) into electromagnetic field expansion expression in Eq.(3.20)-Eq.(3.23), the internal and near field of single sphere can be obtained [74].

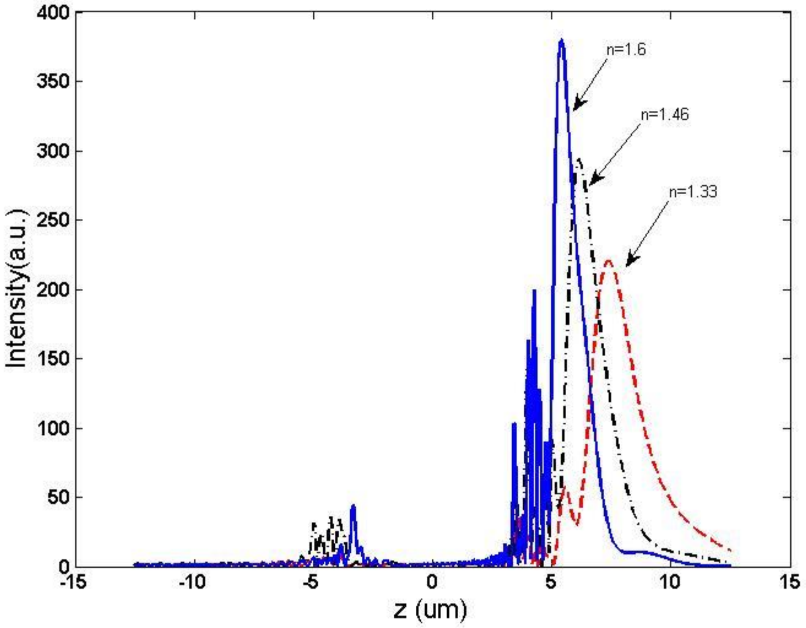

Figure 3. 5 The internal and near field of a sphere ($R = 5\mu m$) with different refractive index at $\lambda = 0.6\mu m$

Considering that the incident plane wave propagates in the direction of the positive z axis and illuminates a sphere with radius $R = 5\mu m$. Figure 3. 5 illustrates the internal and near field distributions of a sphere with different refractive indexes. The wavelength of incident plane wave is

$0.6\mu m$. In this figure, the peaks of maximum intensity shift to center of sphere as refractive index increases for same size of sphere.

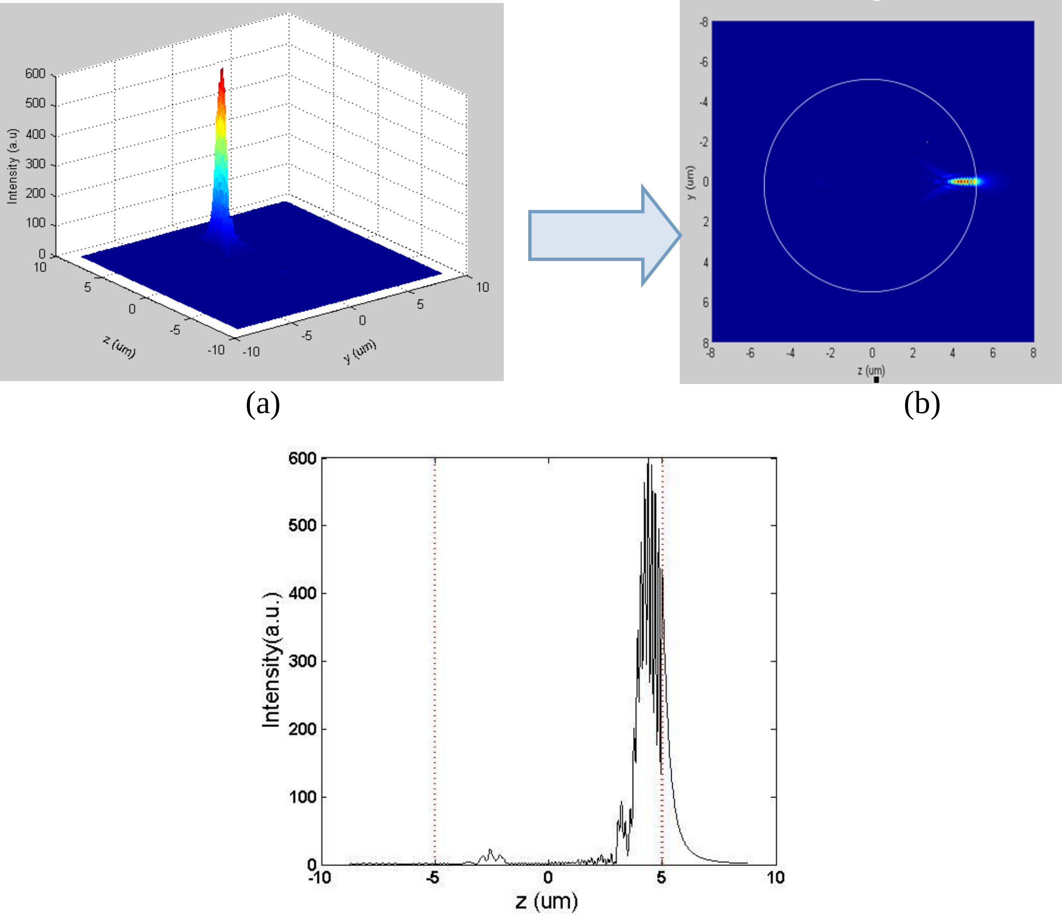

(a) (b)

(c)

Figure 3.6 (a) 3-D plot of the intensity of internal and near field of the microsphere in the y-z plane; (b) corresponding top view from z; (c) corresponding radial internal and near-external intensity distribution of $BaTiO_3$ microspheres along z axis.

Figure 3.6 illustrates near field effects with $BaTiO_3$ microspheres ($R=5\mu m$, $m=1.9$) in air illuminated by plane wave $\lambda = 0.55\mu m$. The three-dimensional intensity pattern of internal and near field of the microsphere in the y-z plane is plotted in Figure 3.6(a). The corresponding diagram view along the negative z axis is shown in

Figure 3.6(b).The radial internal and near-external intensity distribution of $BaTiO_3$ microspheres along z is illustrated in Figure 3.6(c).

It is noted that the red dot line is the location of the surface of sphere, which means intensity between two red line is internal field of the sphere。While in range $x < -5\mu m$, $x > 5\mu m$, intensity is near field, the location of maximum intensity is inside sphere.

3.5 Summary

The EM fields of a sphere illuminated by a plane wave are analyzed based on Mie theory. The expressions for incident, internal and scattered fields expanded in vector spherical functions are given, and the corresponding expansion coefficients are obtained by using the boundary conditions. The scattering intensity distributions of a sphere are calculated, which depend on the size of the sphere, relative refractive index and the incident wavelength. The internal and near field distributions of sphere ($R = 5\mu m$) with different refractive index are computed, and the results show that the peak of maximum intensity widens and shift to center of sphere as refractive index increases. The features of the internal and near field of microsphere are further discussed in Chapter 4.

CHAPTER 4: Application of Mie Theory for Microsphere-based Super-resolution Imaging

Microsphere-based microscopy systems have gained great interests among the scientific communities, mainly due to their capacity in focusing light and imaging beyond the diffraction limit. The simulations of internal and near field show that when the microspheres were illuminated by plane waves, it can produce narrow beams in the near field of the shadow-side surface. Thus microspheres can focus light and enhance the electromagnetic (EM) fields. The super-resolution capability of the spheres stems from its extraordinary sharp focusing properties, so-called “photonic nanojets”. The location and the intensity of photonic nanojets depended on the refractive index contrast between the sphere and their surrounding medium, diameter of the microsphere, and the incident wavelength [75,76, 77, 78, 79, 80, 81]. Also, the focused beams typically have full width at half maximum (FWHM) waists smaller than the incident wavelength and remain sub-wavelength over distances of several wavelengths. This phenomenon has been used to break the diffraction limit in microscopy. In order to increase the spatial resolution of microsphere-based microscopy, the optimal parameters of microsphere are needed to create photonic nanojets with desired resolution.

In this chapter, the influence of the refractive index contrast, the incident plane wave wavelength and the microsphere size on the position of the maximum of photonic jet for microscopy is studied. The FWHM of photonic jet, which relate to the resolution of microscopy, is discussed. The properties of resolution, and magnification with different wavelength, refractive index, microsphere diameter are given. In the following discussion, it is assumed that microspheres have not internal resonances [82,83,84]. Microspheres can be used to focus light with a broad range of wavelengths [85,86].

4.1 Focal Length of Microsphere in Different Conditions

The spatial distributions of the internal and near external electromagnetic fields of plane-wave-illuminated microspheres can be calculated according to discussions in Chapter 3. Suppose that the plane wave (λ=0.6328 μm) propagates along the z axis. The center of the sphere is located on the origin of the coordinate.

Figure 4. 1 shows the electric field intensity of $BaTiO_3$ microspheres (refractive index $m = 1.9$) with radius R=5μm in x-z plane, while the surrounding medium is water (refractive index $m' = 1.33$). The plane wave is incident from the left and impinges on the microsphere. The particle border is represented by a white solid line. The field is highly confined to the surface along the propagation axis z and produces a photonics jet. The corresponding radial internal and near-external intensity distribution of $BaTiO_3$ microspheres along z is shown in Figure 4. 2. For a given unitary incident plane wave, the intensity maximum outside the sphere, which is the focal spot, is multiplied by more than 250. The peak of maximum intensity can be determined as indicated in Figure 4. 2. The calculations have shown that high-intensity peaks exist in both the internal and near-external fields along the incident axis. The location and the intensity of these near-field peaks depend upon the three parameters: refractive index contrast between microsphere and its surrounding medium, the incident wavelength and the diameter of microsphere. And the f (focal length) is defined as the length from sphere center to focal point (projection point of peak intensity on Z axis), as shown in Figure 4. 1 and Figure 4. 2.

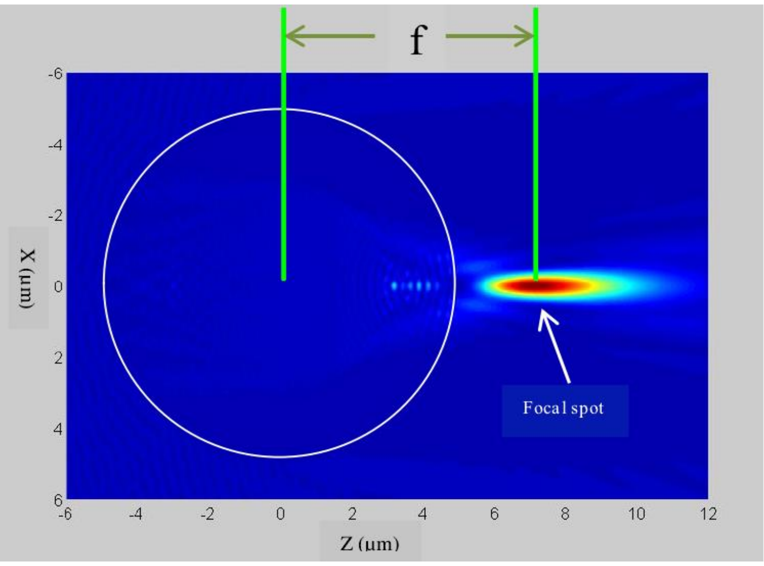

Figure 4. 1 Image of photonic nanojet for wavelength 0.6328 µm, microsphere radius 5 µm and refractive index contrast 1.4286.

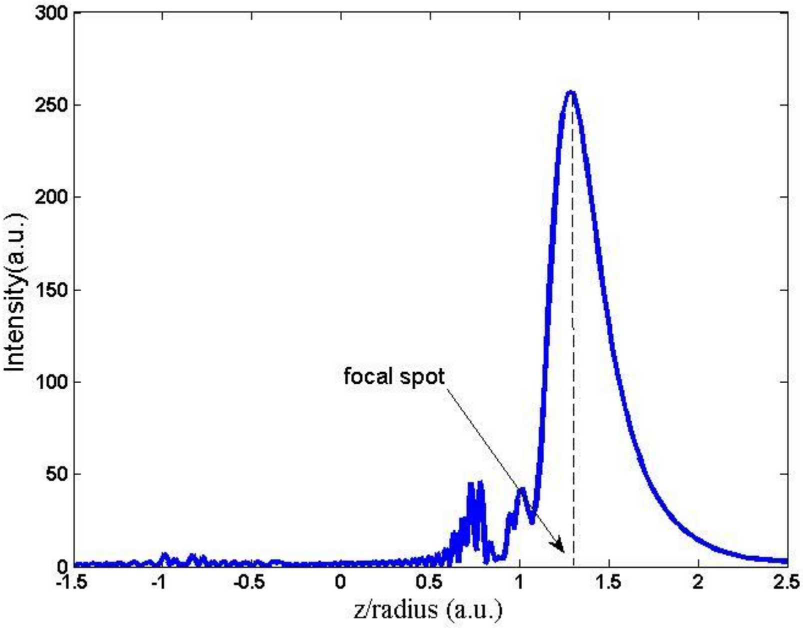

Figure 4. 2 The internal and near-external field distribution for BaTiO3 microspheres, the parameters are the same as in Figure 4.1.

A question arises: how strong is the influence of these parameters on the focal length of the microsphere. The goal of our following work is to find out the influence of focal length on the refractive index contrast, the incident plane wave wavelength and the microsphere radius.

4.1.1 The location of focal spot dependence on wavelength

To be specific, two kinds of microspheres with radius 5 µm, $BaTiO_3$ fused glass microsphere (refractive index $m_1 = 1.9$) and polystyrene microsphere (PS, refractive index $m_2 = 1.6$) are considered.

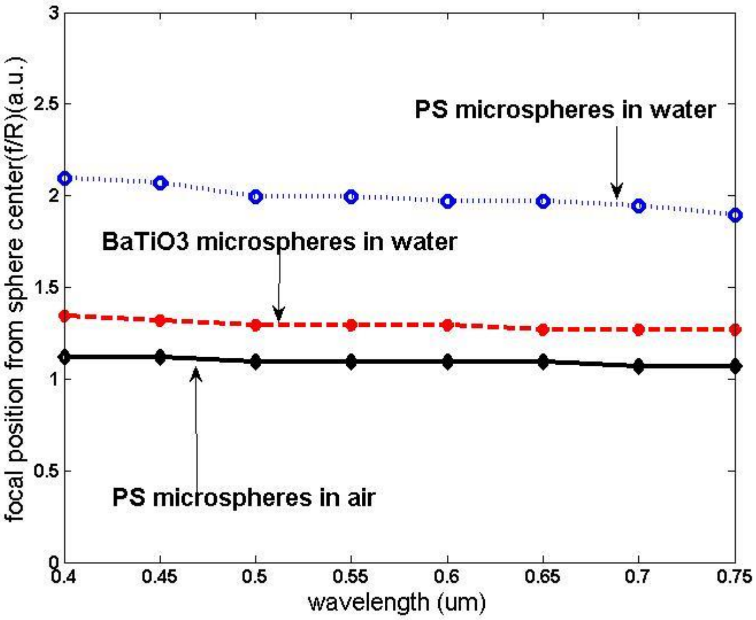

Figure 4. 3 The influence of different wavelengths on the focal position with microsphere radius $R = 5\mu m$. The red curve is for the $BaTiO_3$ microspheres in water, black curve is the PS microspheres in air, and blue curve are PS microspheres in water.

The microspheres are placed in air ($m_0 = 1$) and immersed in water ($m' = 1.33$), respectively. The influence of different wavelengths on the location of focal spot is shown in Figure 4. 3 for $BaTiO_3$ microspheres and PS microspheres with radius $R = 5\mu m$. From Figure 4. 3, while the wavelength increase from 0.40µm to 0.75µm, for the $BaTiO_3$ microspheres in water (red line), the location of focal spot decreases from 1.35R to 1.25R; for the PS microspheres in air (black line) and water (blue line), the location of focal spot decreases from 1.12R to 1.05R, 2.098R to 1.897R. The shift of the focal position caused by wavelength change is less than 6% per micron. The focal positions move toward the center of sphere as wavelength increase.

4.1.2 The location of focal spot dependence on refractive index contrast

The effect of refractive index contrast between the microsphere and the surrounding medium on location of focal spot is shown in Figure 4. 4 with the wavelength λ=0.6328μm and the radius of microsphere $R = 5\mu m$. The focal spot shifts far away from the shadow-side surface of the sphere along the z direction as refractive index decreases. The higher the refractive index contrast, the closer the focal spot to the sphere surface. If the refractive index is too high, the focal spot will be inside the microsphere; if the refractive index is too low, the focal spot is far outside the microsphere. For the radius of microsphere $R = 5\mu m$, the focal spot shift to inside of microsphere when refractive index contrast decreases to 1.84.

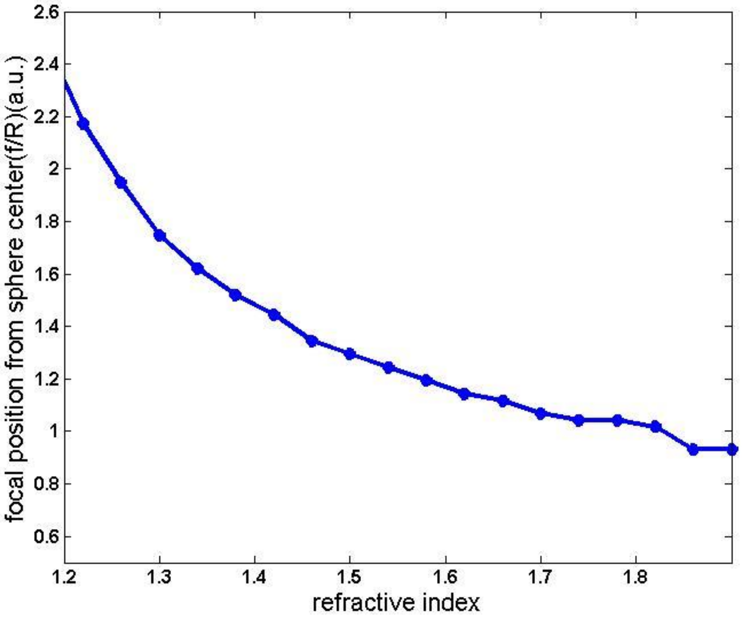

Figure 4. 4 The focal spot shift as a function of refractive index contrast when the λ =0.6328 μm and $R = 5\mu m$.

4.1.3 The location of focal spot dependence on microsphere radius

The location of focal spot is plotted as a function of radius with λ=0.6328 μm, as shown in Figure 4. 5. The red curve is the $BaTiO_3$ microspheres in water, blue curve is PS in air, and black one is PS in water. While radius R of the microspheres increases from λ to 15λ, the focal spot shift far away center of sphere.

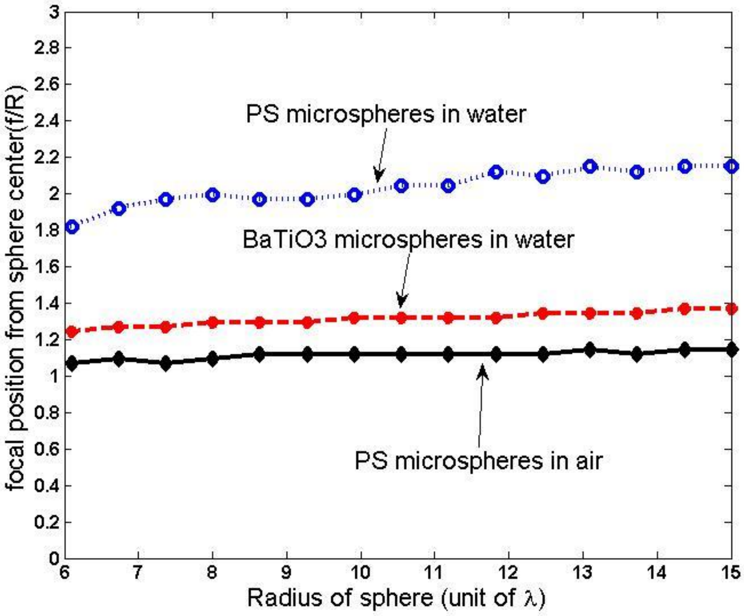

Figure 4. 5 The influence of different radius of the microsphere on the location of focal spot with λ=0.6328 µm.

In conclusion, the influence of different refractive index on the focal spot position is larger than that of wavelength and radius of microsphere.

4.2 The Intensity Distribution of Photonic Nanojet

The effects of the parameters: the refractive index contrast, incident wavelength, and radius of microsphere on the intensity distribution of photonic nanojet, are analyzed. Figure 4. 6 shows the influence on the maximum intensity of photonic nanojet for different refractive index with λ = 0.6328 µm, microsphere radius $R = 5\mu m$. The intensity of nanojet is enhanced compare to incident light. By increasing refractive index, the maximum intensity is more intense. Note that there is a peak in intensity curve at $m = 1.736$ in Figure 4. 6. In the following, photonic nanojets with different refractive index $m = 1.1$, $m = 1.736$, $m = 1.84$, are analyzed respectively to explain this peak.

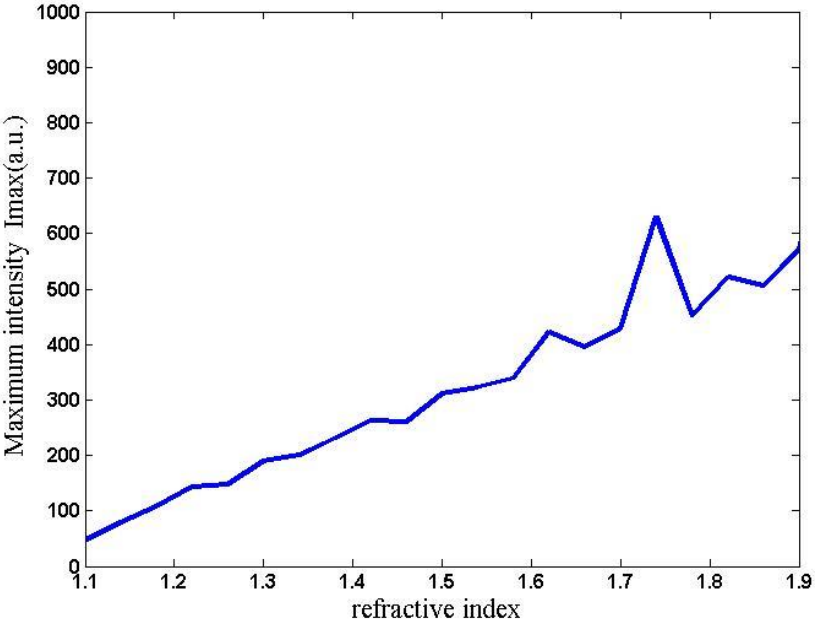

Figure 4. 6 The influence on the maximum intensity of photonic nanojet for different refractive index contrast with λ = 0.6328 μm, microsphere radius $R = 5\mu m$**.**

In Figure 4. 7- Figure 4. 9, three-dimensional photonic nanojets in x-z plane for different refractive index $m = 1.1$, $m = 1.736$, $m = 1.84$ are given with the microsphere radius of $R = 5\mu m$. A plane wave with wavelength λ= 0.6328 μm is incident from the left and impinges on the microsphere. Depending on the refractive index, one see that not only the nanojet dimensions and intensity change but also the separation of the nanojet from the microsphere surface changes. At low refractive index ($m = 1.1$), the nanojet is formed rather far from the shadow microsphere with a lengthening of the nanojet's longitudinal direction along the propagation. The length of the nanojet can be more than 20 micrometers (>30λ), as shown Figure 4. 7.

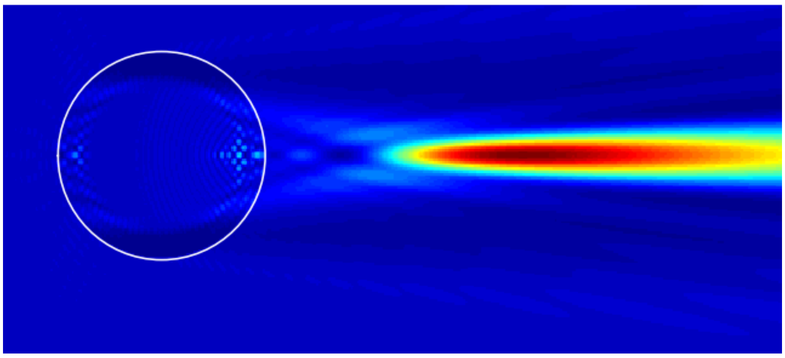

Figure 4. 7 Three-dimensional photonic nanojet in x-z plane for refractive index $m = 1.1$, λ = 0.6328 μm, radius $R = 5\mu m$.

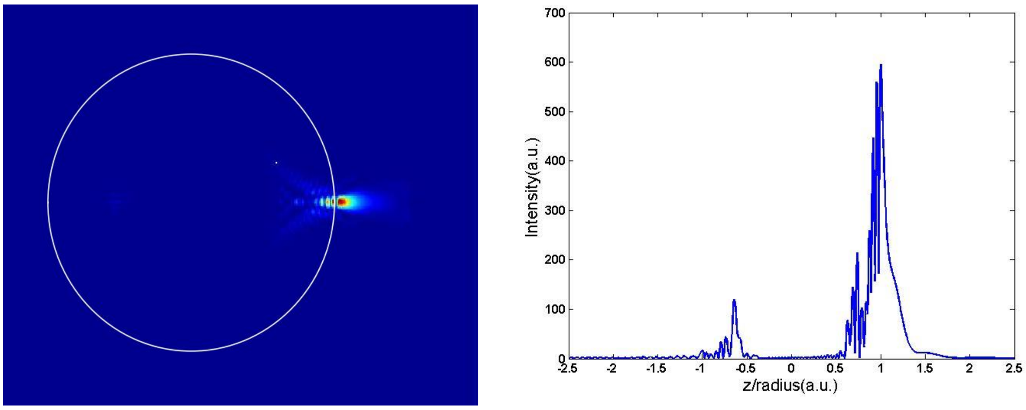

(a) **(b)**

Figure 4. 8 Intensity distribution of microsphere in x-z plane with refractive index $m = 1.736$, λ = 0.6328 μm, radius $R = 5\mu m$. (a) Three-dimensional intensity distribution in x-z plane; (b) The corresponding intensity distribution along the z axis.

At a refractive index $m = 1.736$ the nanojet is close to but still outside the surface of the microsphere with shortening of the nanojet's longitudinal distribution, the maximum intensity and formed the exponentially decaying trail, as shown in Figure 4. 8(a). For The corresponding intensity distribution along longitudinal direction (z axis) is shown in Figure 4. 8 (b). The intensity distribution of nanojet in longitudinal direction becomes more complex. Some spikes appear around primary peak in the radial direction and their widths are smaller. Intensity of nanojet can be enhanced up to 600 times of the incident intensity.

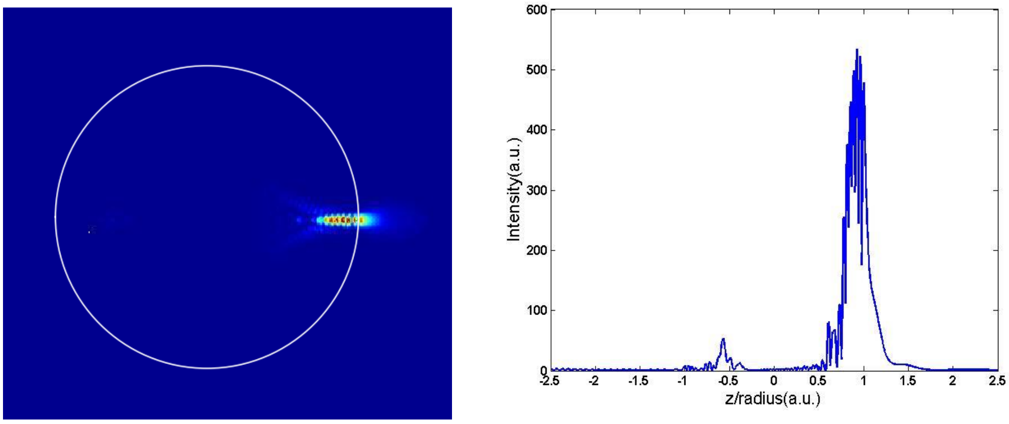

(a) (b)

Figure 4. 9 Intensity distribution of the microsphere with refractive index $m=1.84$, λ = 0.6328 μm, radius $R=5\mu m$. (a) Three-dimensional intensity distribution in x-z plane (b) The corresponding intensity distribution along the z axis.

For refractive index of the microsphere $m=1.84$, three-dimensional intensity distribution in x-z plane is shown in Figure 4. 9(a). The photonic nanojet is inside of the microsphere. There exist some standing-wave-like interferences close to the inner surface of the microsphere. Figure 4. 9 (b) is a plot to show the associated intensity distribution along the z axis. The main intensity profile consists of multiple sharp spikes, which have very narrow width and different intensity. In this case, the photonic nanojet is formed by several focal spots.

In conclusion, the spatial configuration of the photon nanojet depends essentially on the character of refractive index contrast variation. If photonic nanojet is far from surface of the microsphere, it has a lengthened nanojet's longitudinal distribution and a lower intensity; if photonic nanojet is closer to the surface of the microsphere, it has a shortened nanojet's longitudinal distribution and a higher intensity. The reason for peak of curve in the Figure 4. 6 is that photonic nanojet is almost on the surface of the microsphere with highest intensity.

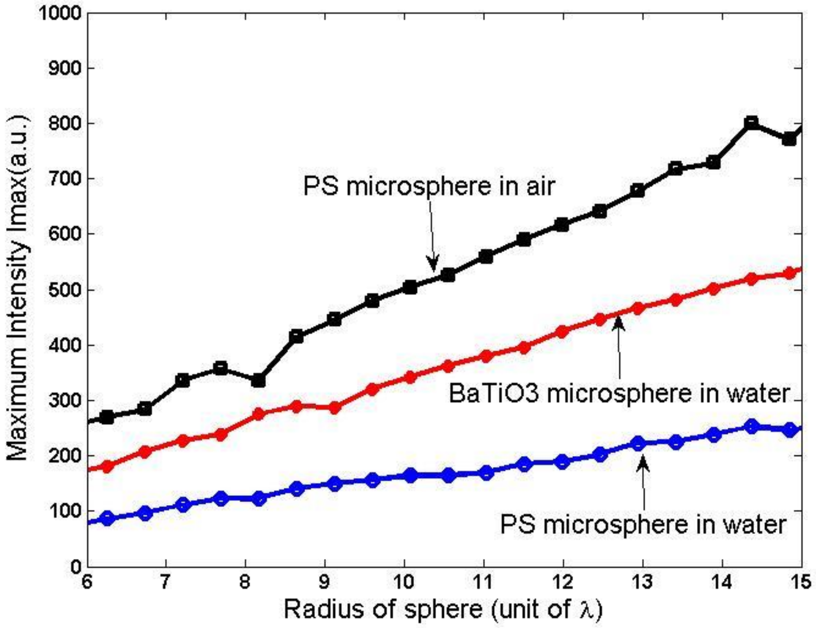

Figure 4.10 The influence on the maximum intensity of photonic nanojet for different microsphere radius with λ = 0.6328 µm.

Furthermore, the photonic nanojet intensity grows with increasing radius of microsphere, as shown in Figure 4.10. For PS microsphere in air, the highest intensity can be achieved at more than 700 time of the incident intensity.

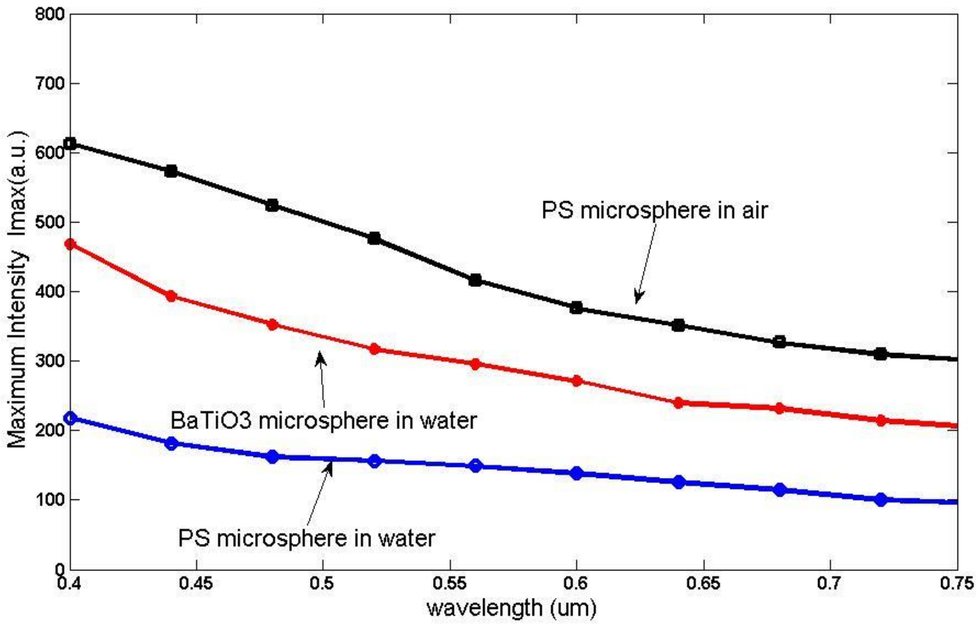

Figure 4. 11 The maximum intensity of photonic nanojet as a function of wavelength with $R = 5\mu m$.

The influence on the maximum intensity of photonic nanojet for different wavelength with $R = 5\mu m$ is shown in Figure 4. 11. While wavelength increases from 0.4µm to 0.75µm, the maximum intensity of photonic nanojet decrease, intensity at λ = 0.75 µm is a half or less than that one at λ = 0.4µm.

4.3 Diffraction Optical Resolution of Microsphere

Now we consider how refractive index, wavelength and radius of microsphere affect the microsphere resolution, which is photonic nanojet's full-width at half maximum (FWHM). As discussed in section 2.1.2, there are several classic criteria defining the spatial resolution of an imaging system, the Houston criterion is more practical among them. According to the Houston criterion [18], two point sources with equal intensities are just resolved if their central distance d is equal to the full-width at half maximum (FWHM) of the intensity distribution of either point source. FWHM is used as the spatial resolution [87,88]. Then, the optical resolution can be determined by Eq. (2.5).

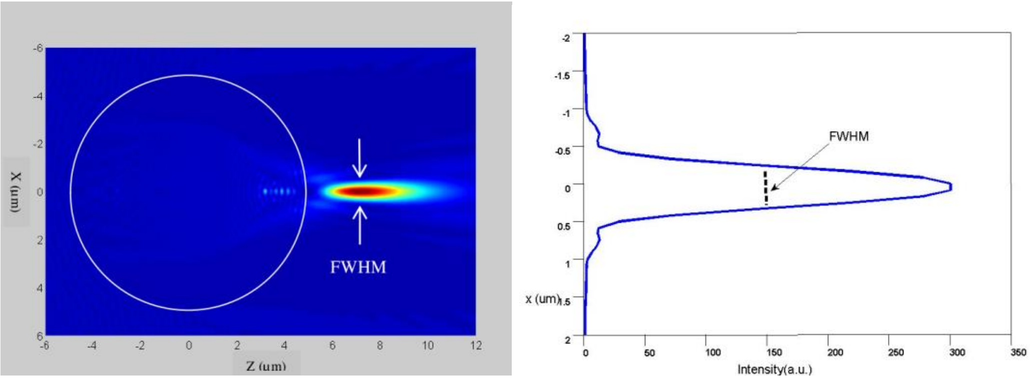

(a) **(b)**

Figure 4.12 (a).Three-dimensional photonic nanojet in x-z plane generated by $BaTiO_3$ microsphere ($m=1.9$) in water with λ = 0.6328 μm, radius $R=5\mu m$, with incident plane wave propagating along z axis. (b) The intensity distribution of photonic nanojet, which is perpendicular to z direction at the focal point.

For $BaTiO_3$ microsphere (refractive index 1.9) in water at λ =0.6328μm, three-dimensional photonic nanojet in x-z plane is observed with the microsphere radius of $R = 5\mu m$ illuminated by a plan wave incident light, as shown in Figure 4.12 (a).

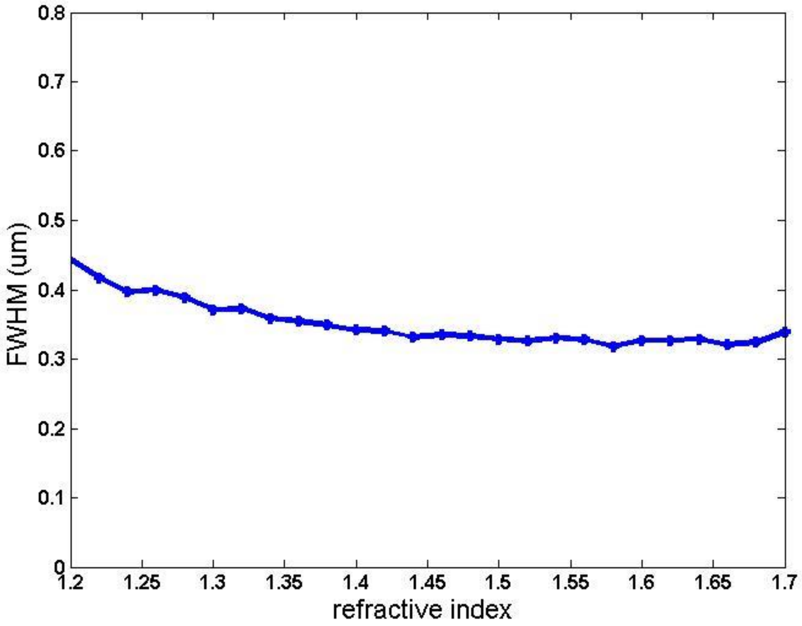

Figure 4. 13 Full-width half-maximum of photonic nanojet as a function of refractive index with λ = 0.6328 μm, microsphere radius $R = 5\mu m$.

The photonic nanojet is generated with narrow and high intensity. The intensity distribution of photonic nanojet, which is perpendicular to z direction at the focal point, is shown in Figure 4.12(b). The corresponding full width at half maximum intensity (FWHM) of photonic nanojet is 0.327 μm. Figure 4. 13 illustrates the dependence of the FWHM of a microsphere with radius $R = 5\mu m$ illuminated at λ= 0.6328 μm on different refractive indices. The FWHM of the photonic nanojet decreases as the refractive index increases. The refractive index changes from 1.2 to 1.7.

Figure 4. 14 shows FWHM at different radius of microspheres. For a PS microsphere in water, the peak intensity of photonic nanojet is higher and FWHM is wider as microsphere radius increase, shown in Figure 4. 14 (a). Also the FWHM increase as size of microspheres increase, shown in Figure 4. 14 (b).

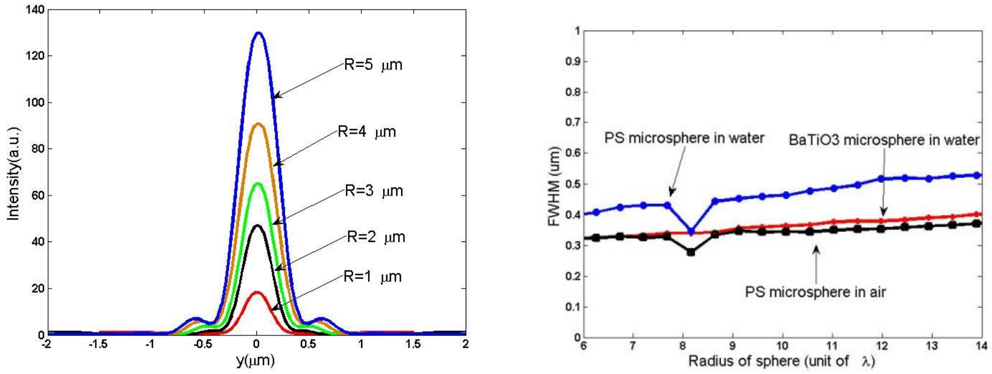

(a) **(b)**

Figure 4. 14 The FWHM as functions radius of microspheres with λ = 0.6328 µm. (a) The FWHM for PS microspheres in water with radius $R = 1\mu m$, $R = 2\mu m$, $R = 3\mu m$, $R = 4\mu m$, $R = 5\mu m$, respectively; (b) The FWHM for different microspheres with radius from 6λ to 14λ. Black curve is PS microspheres in air, and blue curve is that in water. Red curve shows $BaTiO_3$ microspheres in water.

The influence of different wavelengths on the FWHM for $BaTiO_3$ and PS microspheres with radius $R = 5\mu m$ is shown in Figure 4.15. While wavelength decreases from 0.4 µm to 0.7 µm, the FWHM increases from 0.24 µm to 0.38 µm for $BaTiO_3$ microspheres in water, and from 0.23 µm to 0.36 µm for PS microspheres in air.

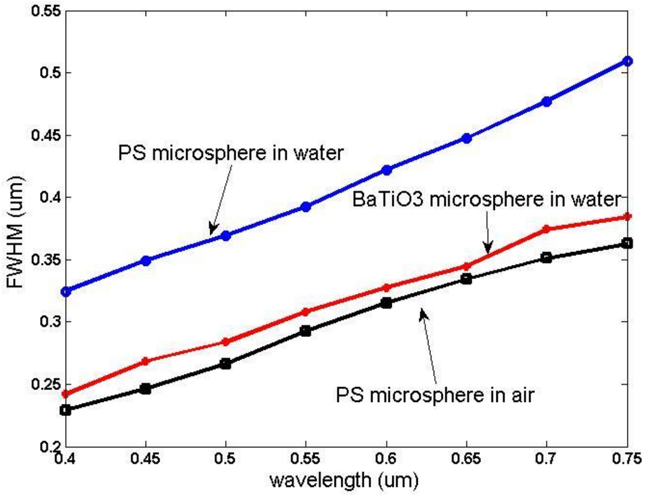

Figure 4.15 The influence of different wavelengths on the FWHM with microsphere radius $R = 5\mu m$. Black curve is PS microspheres in air, and blue curve is that in water. Red curve shows $BaTiO_3$ microspheres in water.

4.4 Example of PS Microsphere with Radius 2.5 µm

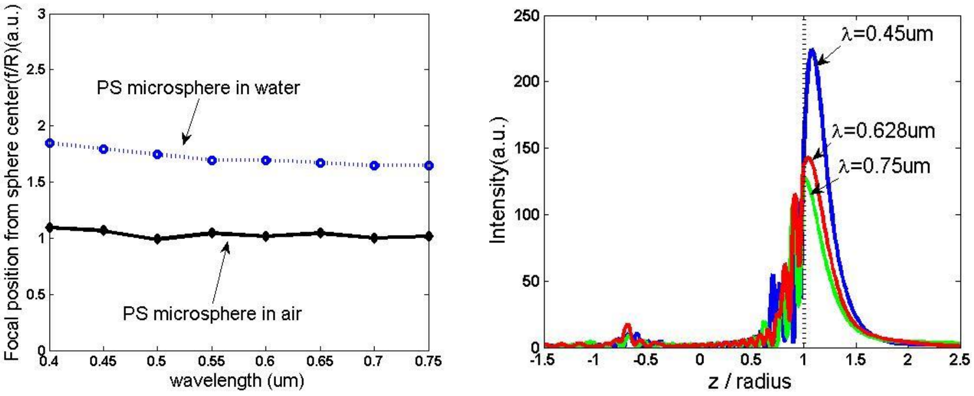

(a) (b)

Figure 4. 16 (a). The influence of different wavelengths on the location of focal spot with microsphere radius $R = 2.5\mu m$. The black curve is the PS microspheres in air, and blue curve are PS microspheres in water. (b) The internal and near field of PS microspheres in air ($R = 2.5\mu m$) with different wavelengths.

As example, the polystyrene microsphere (PS, refractive index $m_2 = 1.6$) with radius 2.5 µm are used. The microsphere is placed in air ($m_0 = 1$) or immersed in water ($m' = 1.33$), respectively.

The influence of different wavelengths on the location of focal spot is shown in Figure 4. 16. While the wavelength increase from 0.40µm to 0.75µm, for the PS microspheres in air (black line) and water (blue line), the location of focal spot decrease from 1.09R µm to 1.02R µm, 1.85R µm to 1.65R µm, respectively. The focal positions of PS microspheres in air are very close to the surface of microsphere and move toward the center of sphere as wavelength increase, shown in Figure 4. 16(b).

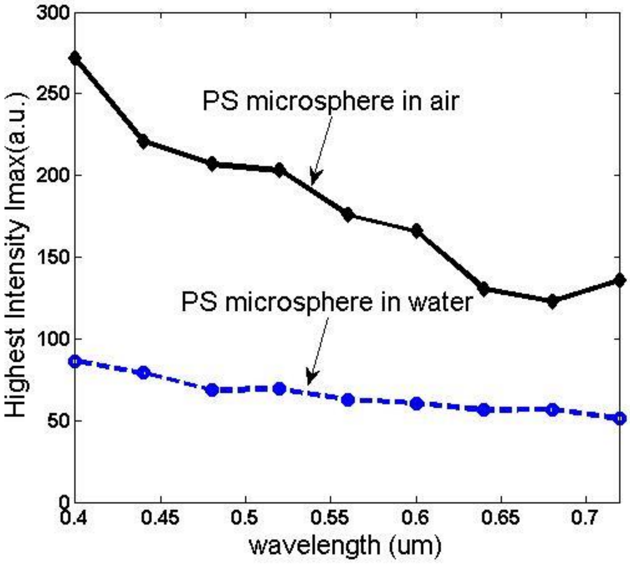

Figure 4. 17 The maximum intensity of photonic nanojet as a function of wavelength with $R = 2.5\mu m$**.**

The photonic nanojet intensity decreases with increasing wavelength. For PS microsphere in air, the highest intensity can be achieved more than 270 time of the incident intensity, shown in Figure 4. 17. When PS microsphere is in water, the location of focal spot are far away center of microsphere, and the photonic nanojet intensity is lower.

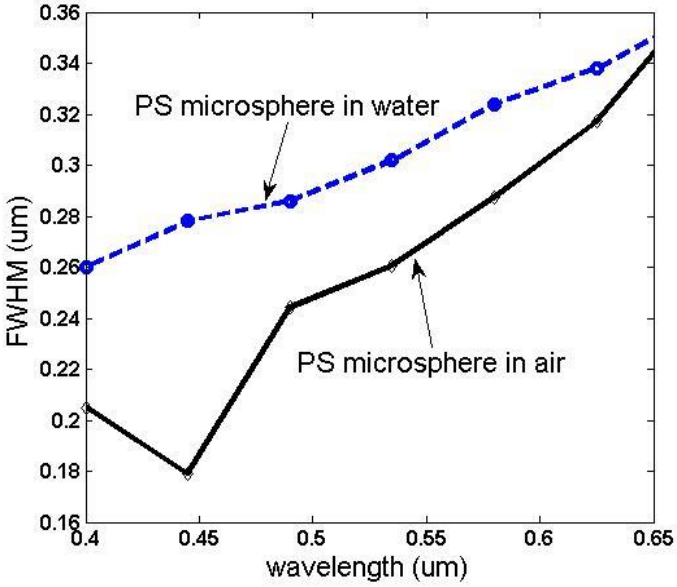

Figure 4. 18 The influence of different wavelengths on the FWHM with microsphere radius $R = 2.5\mu m$. Black curve is PS microspheres in air, and blue curve is that in water.

Figure 4. 18 graphs the influence of different wavelengths on the FWHM for PS microspheres with $R = 2.5\mu m$. The FWHM is less than half wavelength for PS microspheres in air, which means optical resolution of PS microspheres in air is lower than the diffraction limit.

4.5 Summary

To provide explanation for the super-resolution of microsphere-based microscopy, based on Mie theory, the super-focusing effects of photonic nanojet have been studied. Intensity distributions in the 3D and 2D photonic nanojets have been simulated based on microsphere illuminated by a plane wave. The simulation results show that sub-diffraction focus beam is generated at the shadow side of microsphere. The maximum intensity of the nanojet increases with increasing the size of the microsphere and refractive index of the surrounding, and the Full-width half-maximum of photonic nanojet decrease simultaneously. The highest intensity outside the microsphere is reached when the focus point is close to the surface of the microsphere. Intensity can be enhanced up to 900 times of the incident intensity. Analysing these numerical results will allow to optimise the wavelength and the refractive indices so that the FWHM can be minimised. A photonics jet with higher resolution can be used to improve optical resolution for microscopy and observe or manipulate of nano-objects.

CHAPTER 5: The Properties of Microsphere Imaging

5.1 Image Position and Magnification of Microsphere

From the view of geometrical optics, the microsphere is the thick lens, and the images can be formed by a microsphere. The imaging plane position and image magnification factor can be given by considering the spherical lens effect and spherical aberration, as follows [2]:

$$l' = -\frac{(R+\delta)f}{f-R-\delta} \tag{5. 1}$$

$$\beta = \frac{f}{f-R-\delta} \tag{5. 2}$$

where is l' the imaging plane position from the center of the microsphere, β is the microsphere image magnification factor, f is the focal length of the microsphere from the sphere center, δ is the distance from the target to the microsphere surface.

For visible light, the focal position for PS microsphere in water is 0.482µm from surface of microsphere with R=5µm, λ = 0.6328µm, as shown in Figure 5. 1.

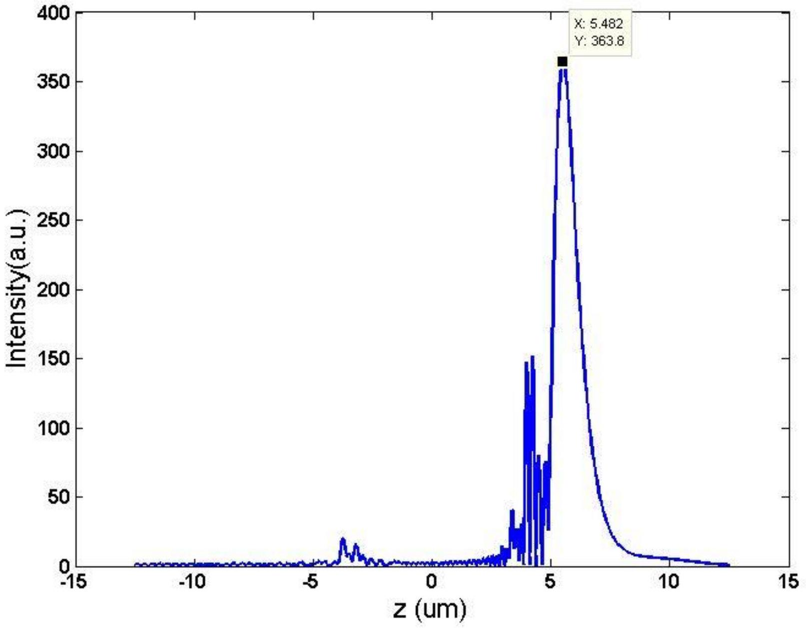

Figure 5. 1 Intensity distribution of PS microsphere in air with $R = 5\mu m$, λ = 0.6328 µm, the focal position is 0.482µm from surface of microsphere, based on Mie Theory.

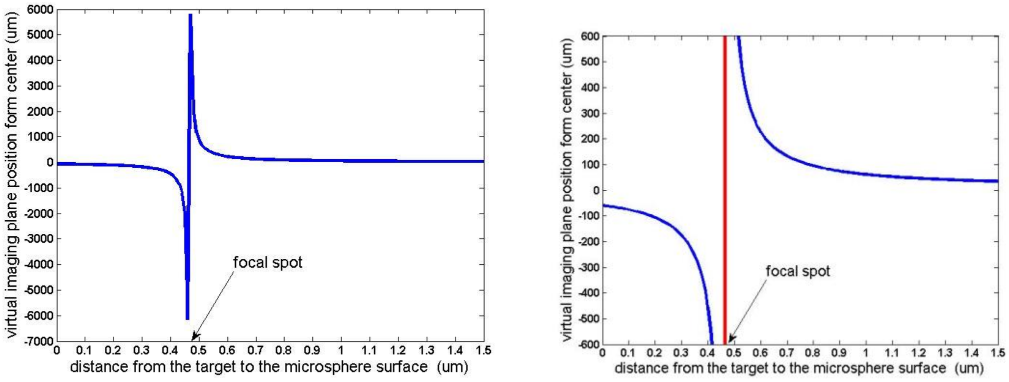

(a) **(b)**

Figure 5. 2(a) The image distance as functions of object distance. (b) The image distance around focal point is zoomed, based on Eq. 5.1.

When an object is inside the focal point of microsphere, that is, object distance is smaller than 0.482 µm, the image distance is negative and located on the same side of the microsphere as the object, shown in Figure 5. 2. Figure 5. 2(a) shows the image distance as functions of object distance, Figure 5. 2(b) is zoomed around the focal point area.

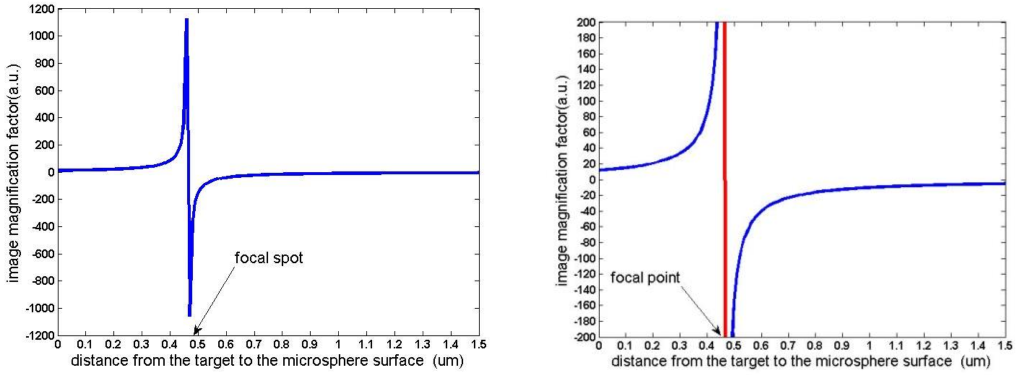

(a) **(b)**

Figure 5. 3 (a) The magnification as functions of object distance. (b) The magnification around focal point is zoomed, based on Eq. 5.2.

The image distance increases as the object is closer to focal point. The image is virtual, upright, and larger than the object. The corresponding magnification is positive, and grows as object distance is closer to focal point, as shown in Figure 5. 3. While an object placed outside the focal point of microsphere, that is, object distance is larger than 0.482µm, the image distance is positive, and the image's position is located on the opposite side of the object. As the object is closer to focal point, image is real and inverted, the relevant magnification is negative, as in Figure 5. 3. When the object is closer to focal point, absolute value of magnification increase, the image is moved farther away. Note that object is placed at focal point, image should be at infinity. So, the curves have high peak in Figure 5. 2 and Figure 5. 3, which mean that the object's position is very close to focal point.

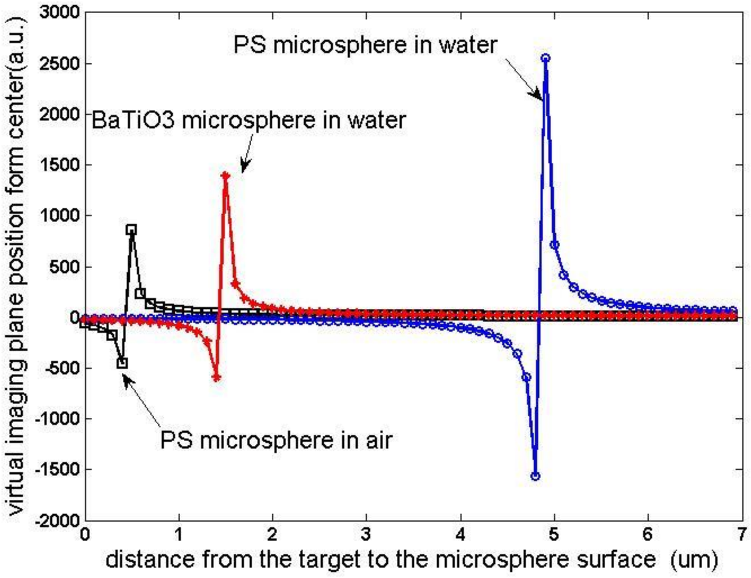

Figure 5. 4 The image distances for PS and $BaTiO_3$ microspheres at different refractive index contrasts.

Figure 5. 4 and Figure 5. 5 compare the image distances and magnification for PS and $BaTiO_3$ microspheres with different refractive index contrast. For microspheres in water, the focal position are 4.81 µm away from the surface for PS, and 1.42 µm for $BaTiO_3$ .The properties of image are similar to that of PS microspheres in air, but the ranges of image distance and magnification are larger. For example, the image distance and magnification for PS microspheres in water is

zoomed with range of object distance from 0 µm to 4.5 µm, as shown in Figure 5. 6 (a) and (b), while object distance changes from 0 µm to 4.5 µm, the image move far away from -10.14 µm to -103 µm, which is on the same side of the object, and the relevant magnification is from 2.0 to 11.44.

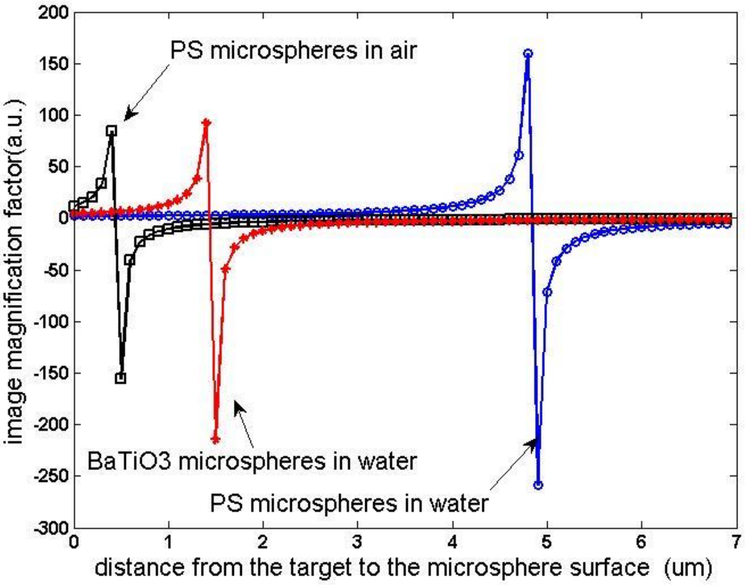

Figure 5. 5 The magnification for PS and $BaTiO_3$ microspheres at different refractive index contrasts.

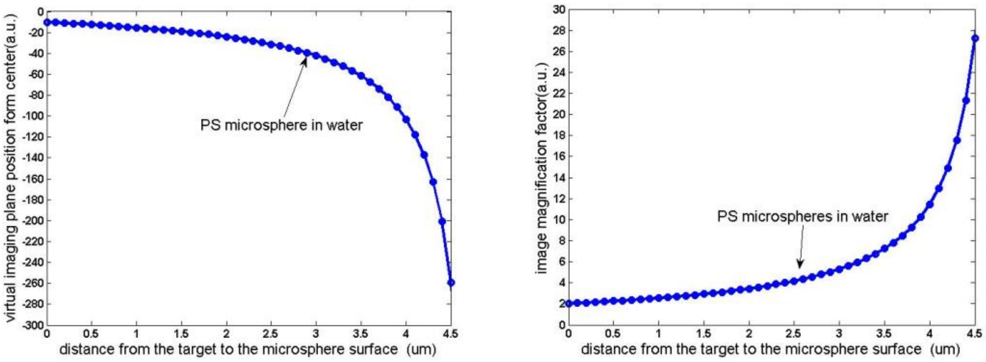

(a) **(b)**

Figure 5. 6 The object distance of PS microspheres in water changes from 0 µm to 4.5 µm, (a) the image distance as functions of object distance; (b) magnification as functions of object distance

5.2 The Magnification in Different Conditions

Bases on computation for focal length of the microsphere in Chapter 4, focal length of the microsphere is determined by three parameters, the refractive index contrast surrounding medium, the incident plane wave wavelength and the microsphere size. So, the magnification of microsphere also depends on those parameters.

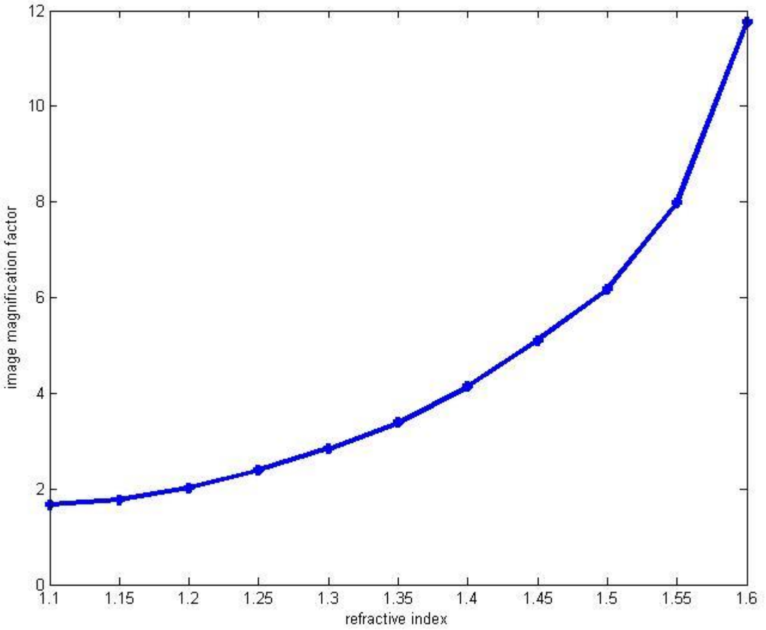

Figure 5. 7 The influence of the refractive index contrast on the magnification of microsphere with $R = 5\mu m$, λ = 0.6328 μm, $\delta = 0$.

Suppose that the object is very close to surface of microsphere, that is $\delta = 0$, Figure 5. 7 shows the influence of the refractive index contrast on the magnification factor. The magnification increase more than 40 times while the refractive index change from 1.1 to 1.7 with microsphere radius $R=5\mu m$ μm, λ = 0.6328 μm.

The magnification as functions of microsphere radius is shown in Figure 5. 8 with λ=0.6328μm. As the size of microsphere increases, the magnification decreases. The magnification of PS microsphere in air is larger because the object is close to focal point of PS microsphere.

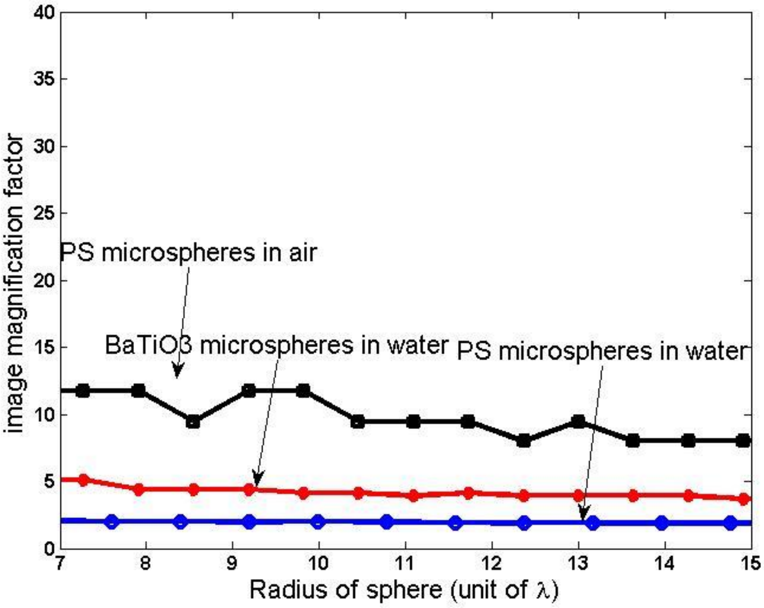

Figure 5. 8 The magnification as functions of microsphere radius with λ = 0.6328 μm, $\delta=0$

Figure 5. 9 shows the influence of wavelength on the magnification for microsphere with R =5 μm. Magnification grows as the wavelength increases. The influence of different refractive index on the magnification is larger that of wavelength and radius of microsphere.

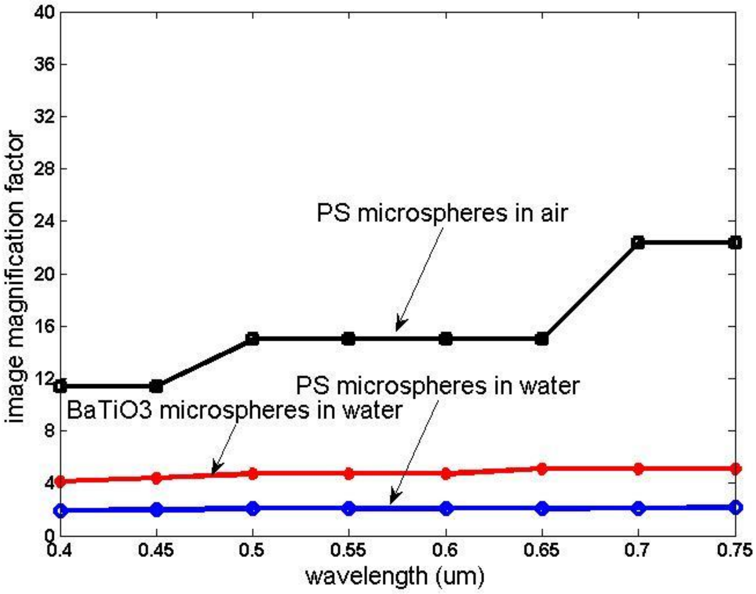

Figure 5. 9 The magnification for microsphere as functions of wavelength with $R = 5\mu m$, $\delta = 0$.

5.3 Approximate Method for the Magnification

In our discussion above, if the object is very close to focal point, the magnification becomes extremely large, even infinite, the results of magnification in geometrical optics become invalid. For example, the focal position of SiO_2 microsphere with $R = 1.2$ from surface is 0.0μm approximately for λ= 0.6, when object is placed on the surface of microsphere ($\delta = 0$), the magnification by using Eq.(5.2) is (-3.3×10^5), which is invalid obviously. The focal position of PS in air is just around the surface of microsphere, when the object is placed on the surface ($\delta = 0$), the image magnification factor appears some fluctuation, as the black curve shown in Figure 5. 8 and Figure 5. 9.

Wang et al proposed that the virtual image magnification depends on the maximal field enhancement produced by the microspheres [3]. Based on geometrical optics approximations, virtual image magnifications β are calculated by fitted formula (2 µm < diameter < 9 µm, $m = 1.46$):

$$\beta \approx (\frac{I_{\max}}{I_0})^{\sigma} \tag{5. 3}$$

where the factor $\sigma = 0.34$ is given by Ref [3]. As object is placed on surface of microsphere with $m = 1.46$ and λ= 0.6 µm, the $I_{\max}$ can be computed by Mie theory, which is discussed in Section 4.2. The magnification is calculated by using approximations formula Eq.(5.3), as shown in Figure 5. 10 (b). Figure 5. 10 (a) is magnification given by Ref. [3]'s Fig.4 (d), which $I_{\max}$ is computed by geometrical optics approximation [3,89]:

$$(\frac{I_{\max}}{I_0}) = \frac{27m^4}{(4-m^2)^3}\left[\begin{array}{cc} 1 & m < \sqrt{2} \\ \dfrac{m^2}{2m(m-\sqrt{2})+2} & m > \sqrt{2} \end{array}\right. \tag{5. 4}$$

Two results are in good agreement. The magnifications, calculated by Wang's approximations formula, as functions of refractive index for different microsphere radius with λ = 0.6 μm are given in Figure 5. 11. The magnifications increase as refractive index grows.

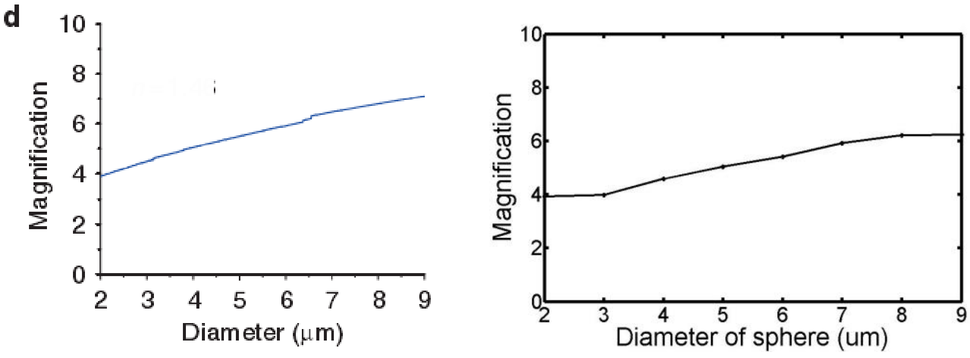

(a) **(b)**

Figure 5. 10 The magnification for microsphere with $m = 1.46$, λ= 0.6 μm, is calculated by Wang's approximations formula. (a) $I_{\max}$ is calculated by geometrical optics approximation in Fig.4(d) of Ref.[3]'s; (b) $I_{\max}$ is calculated by Mie theory.

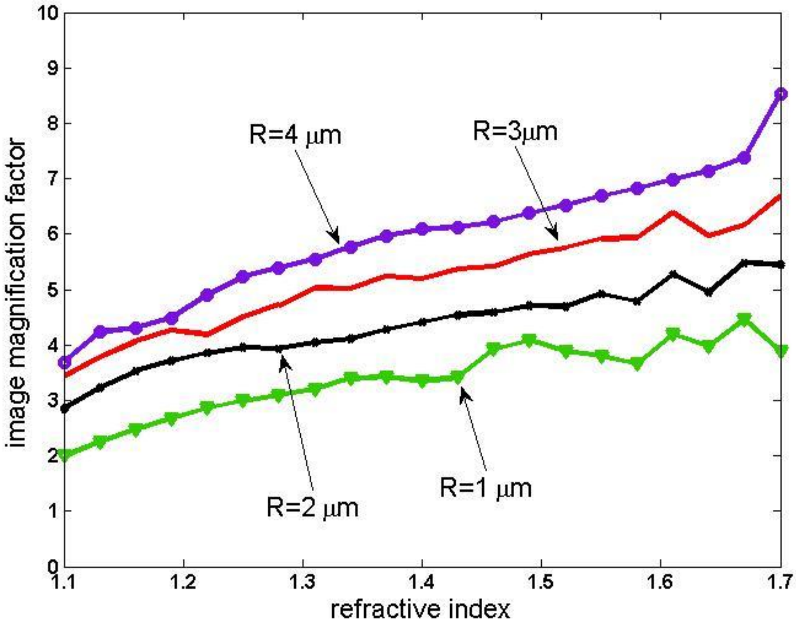

Figure 5. 11 The magnifications as functions of refractive index for different microsphere radius with λ = 0.6 μm.

5.4 Error Analysis for Difference of Focal Length between Geometrical Optics and Mie Theory

When the microspheres are illuminated by plane waves, they can focus light and enhance the electromagnetic (EM) field. This resembles the focusing effect of a lens. In geometrical optics, microsphere is considered as a thick lens. Considering the spherical lens effect and spherical aberration, the focal length of the microsphere from the sphere center f_{GO} is given [2]:

$$f_{GO} = \frac{l}{\sin\left\{ \; 2\sin^{-1}(l/R) - 2\sin^{-1}[(m_0/m_1)(l/R)] \; \right\}} \tag{5. 5}$$

where l is the transverse distance from the optical axis, R is the microsphere radius, m_0 is the ambient refractive index, m_1 is the refractive index of the microsphere. However, the properties of such focal spots by Mie theory, such as intensity, position, magnifications, are distinct from those predicted by geometrical optics (GO).

The relative error of focal length is defined as

$$\Delta = \frac{f_{GO} - f_{Mie}}{f_{GO}} \tag{5. 6}$$

where f_{Mie} is focal length determined by Mie theory in chapter 4.

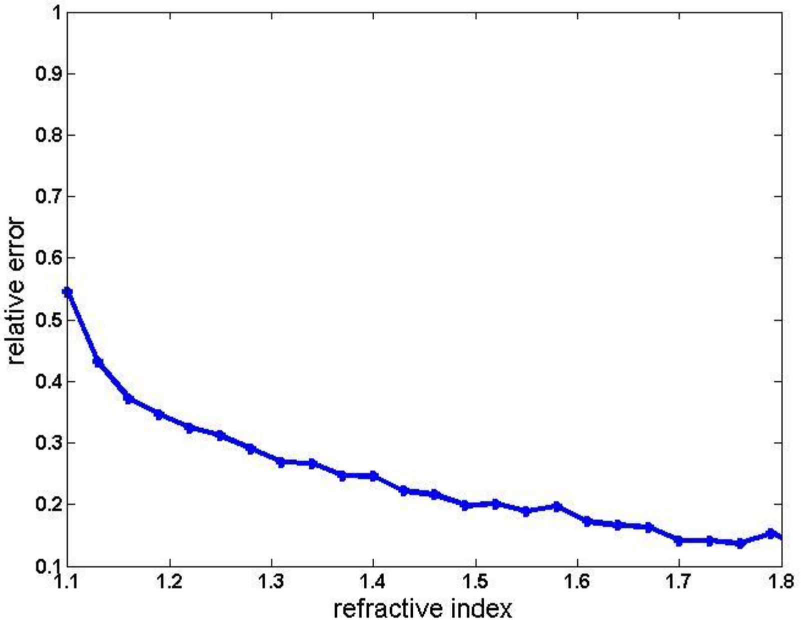

Figure 5. 12 Relative error of focal length as a function of refractive index contrast with R=5 μm, λ = 0.6328 μm, l=0.01 μm.

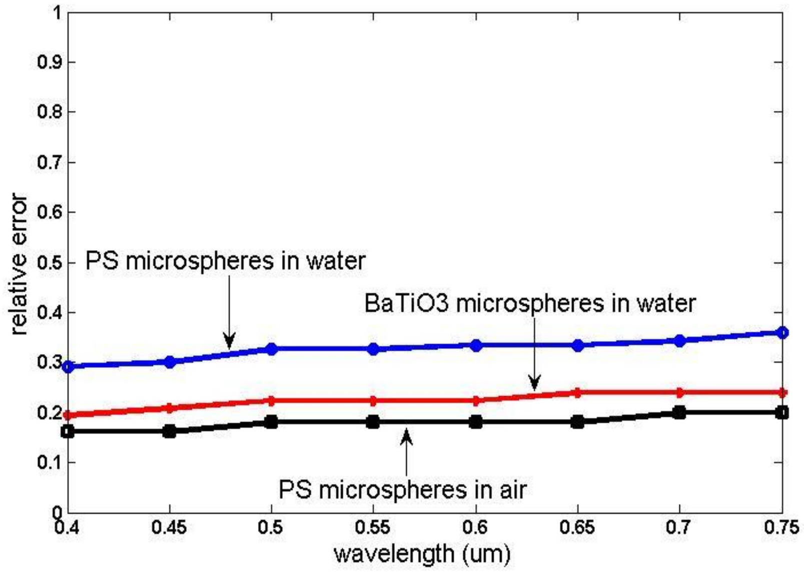

Figure 5. 13 The relative error of focal length as a function of wavelength with R=5 μm, l=0.01 μm.

For a given R=5 μm, λ = 0.6328 μm, l=0.01 μm, Figure 5. 12 compares relative error of focal length as a function of refractive index contrast, the lower is refractive index, the higher is the relative error for the microsphere. The maximum relative error is about 55% at $m = 1.1$ for this case.

Figure 5. 13 shows the influence of wavelength on the relative error of focal length with R=5 µm, l=0.01 µm. The relative error is less than 40 % for PS microsphere in air or in water and less than 25 % for $BaTiO_3$ microsphere in water.

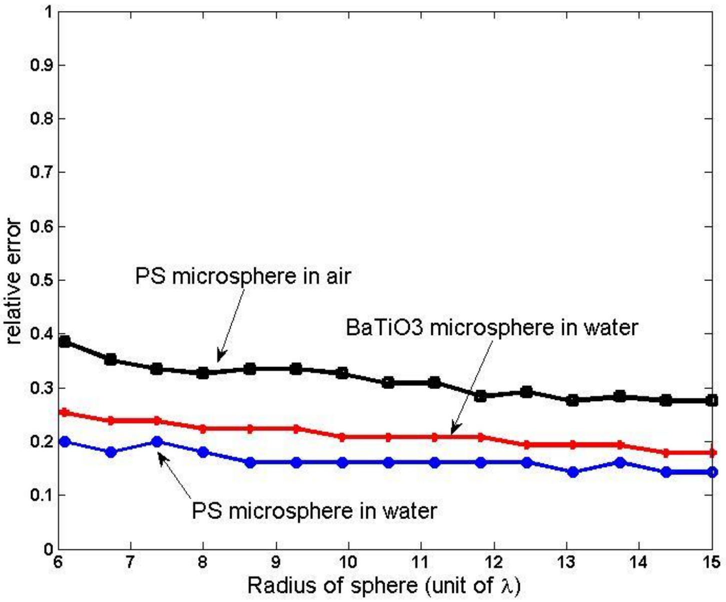

Figure 5. 14 The relative error of focal length as a function of microsphere radius with λ = 0.6328 µm, l=0.01 µm

The relative error of focal length as a function of microsphere radius is given in Figure 5. 14 with λ = 0.6328 µm, l=0.01 µm, the influence of microsphere size on the relative error is lower than 40%. As the microsphere size increases, the relative error becomes small, because if light propagates through a very larger microsphere, the results of Mie theory are close to that of geometrical optics.

5.5 Summary

Bases on Mie theory, the imaging plane position and image magnification factor are discussed by using the geometrical optics. The properties of the image distances and magnification for microspheres with different refractive index contrast, wavelength and radius are given. As the object is very close to focal point, the results of magnification in geometrical optics become invalid, the virtual image magnification, which depends on the maximal field enhancement produced by the microspheres, are calculated based on geometrical optics approximations. The focal spots positions of microsphere predicted by Mie theory, are different from those predicted by geometrical optics (GO). A detailed comparison of the focal lengths by using two theories is given, the corresponding relative errors are discussed.

CHAPTER 6: Comparison of Theoretical and Experimental Results

It is clear from previous discussion that a microsphere can focus an incident plane wave. Depending on parameters of microsphere, medium and incident wave, the focus point can be inside or outside the sphere. As the focus point of microsphere is close to the surface of the sphere, the full width at half-maximum of the focus point becomes smaller than the half a wavelength. Using microsphere capacity in focusing light and imaging, microsphere-based microscopy systems have been developed in recent year, and the highest spatial resolution beyond the diffraction limit can be achieved [2,3,46,47,90,91,92].

6.1 Microsphere-based Microscopy

Z Wang presented 50-nm-resolution microscopy that uses silica spheres with a refractive index m =1.46. and with diameters in the range 2µm< D <9µm to overcome the light diffraction limit and obtain high resolution [3].The microspheres are placed on the top of the object surface, the object was Blu-ray DVD disk which has 200-nm-wide stripes separated 100 nm apart, as shown in Figure 6.1.

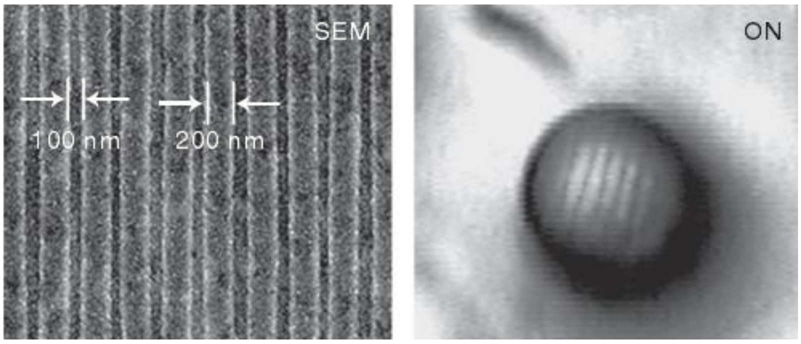

Figure 6.1 Microsphere (R = 2.37 µm, $m=1.46$) is placed on Blu-ray DVD disk (200-nm-wide lines separated 100 nm apart). The sub-diffraction-limited 100 nm lines (left image) are resolved by the microsphere (right image) with λ = 0.6 µm [3].

The experiment demonstrates that a microsphere was able to focus light down to sub-diffraction-limited dimensions. Using Mie theory, three-dimensional photonic nanojet in x-z plane is obtained for microsphere (R=2.37 µm, $m=1.46$, λ = 0.6 µm), as shown in Figure 6.2 (a). The corresponding radial internal and near-external intensity distribution of microspheres along z is shown in Figure 6.2 (b). The focal spot from sphere surface is 0.35 µm. The ratio of maximum intensity to incident intensity of the microspheres is 105.67, so, the magnification by using Wang's approximations formula, which depends on the maximal field enhancement produced by the microsphere, is 4.9. The full width at half maximum intensity of photonic nanojet for this microsphere is 0.288µm, illustrated in Figure 6.3, and is lower than one-half of the incident wavelength 0.3 µm, which indicates that the diffraction limit is overcome.

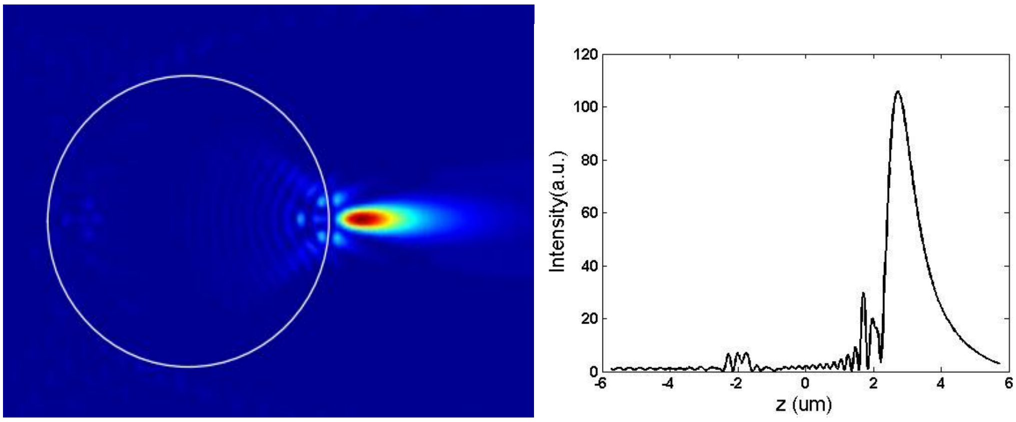

(a) (b)

Figure 6.2 (a) Three-dimensional photonic nanojet in x-z plane for microsphere (R=2.37 μm, $m = 1.46$, λ = 0.6 μm); (b) The corresponding radial internal and near-external intensity distribution of microspheres along z.

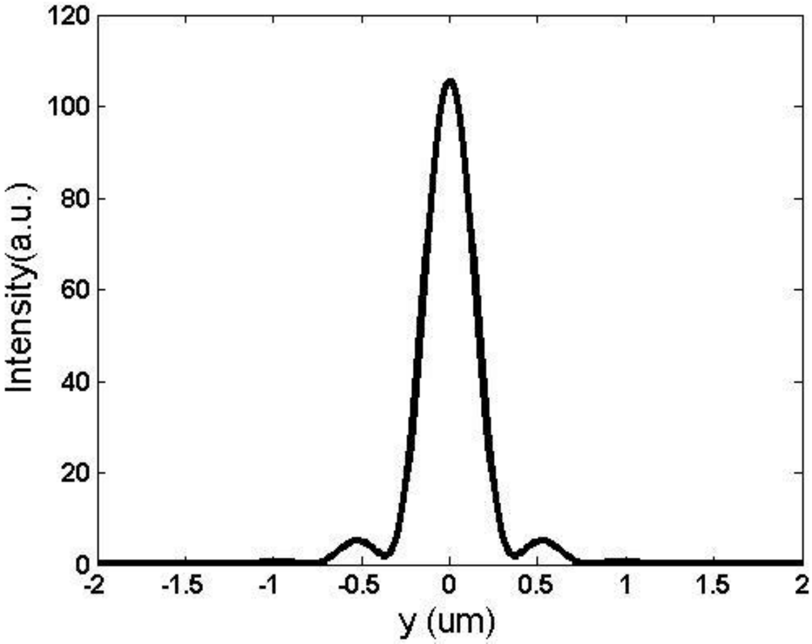

Figure 6.3 The full width at half maximum intensity of photonic nanojet for microsphere, the parameters are same as Figure 6.2.

6.2 Super-resolution by Liquid-immersed Microspheres

As discussion in section 4.1.2 and 4.2, if the index contrast of microsphere is larger than 1.84, the focal point is inside the microsphere. Then the object is placed outside the focal point of microsphere, so the image is real and inverted. And the image's position is on the opposite side of the object, the magnification of image is too small to discern the object. Darafsheh et al experimentally demonstrate that high index $m \sim 1.9-2.1$ microspheres did not produce any imaging [46].

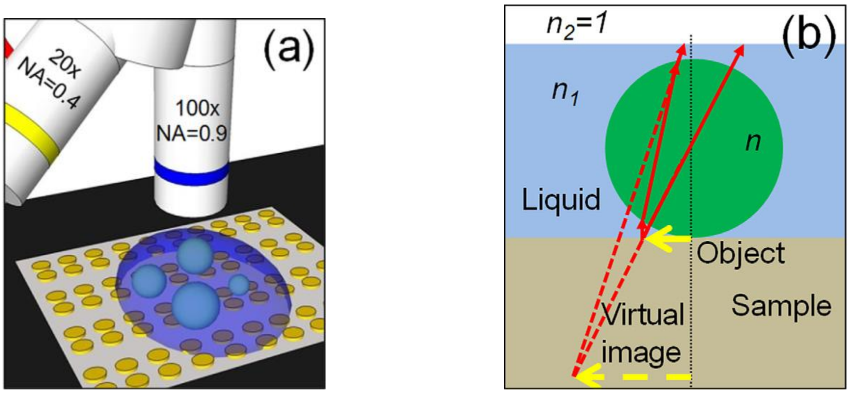

(a) (b)

Figure 6.4 (a) Experimental configuration of the setup nanoscope. (b) Virtual image formation by a liquid-immersed microspheres [46].

Some methods are presented, such as semi-immerse or total- immerse the microsphere in the liquid, to make the relative refractive index less than 1.84 when using high index microspheres [43,46,48]. Darafsheh et al obtained the super-resolution imaging experimentally by microspheres totally immersed in the liquid [46,93].

The configuration and a virtual image formation are illustrated in Figure 6.4 (a) and (b), respectively [46]. The barium titanate glass (BTG) microspheres with a refractive index $m \sim 1.9-2.1$ are immersed in isopropyl alcohol (IPA) with index $m_0 = 1.37$. The peak illumination wavelength is 0.550 µm.

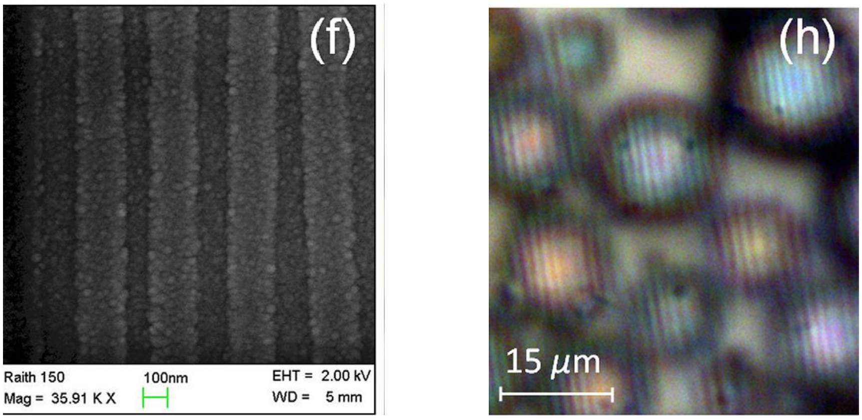

(a) **(b)**

Figure 6.5 (a) SEM image of a Blu-ray disk; (b) Virtual imaging of the Blu-ray disk through the microspheres with diameters in the range ~5-20 µm fully immersed in IPA [46].

One of the samples is a commercial Blu-ray disk with track pitch sizes of 0.3µm consisting of 0.2µm width stripes separated by 0.1 µm width grooves, as shown in Figure 6.5(a). The microspheres with diameters in the range 5-20 µm were placed on the sample and totally covered by IPA. It is seen that the virtual images of Blu-ray disk are resolved in Figure 6.5 (b). The results show that high-index liquid-immersed spheres have super-resolution capability due to photonic nanojet properties of microspheres [46].

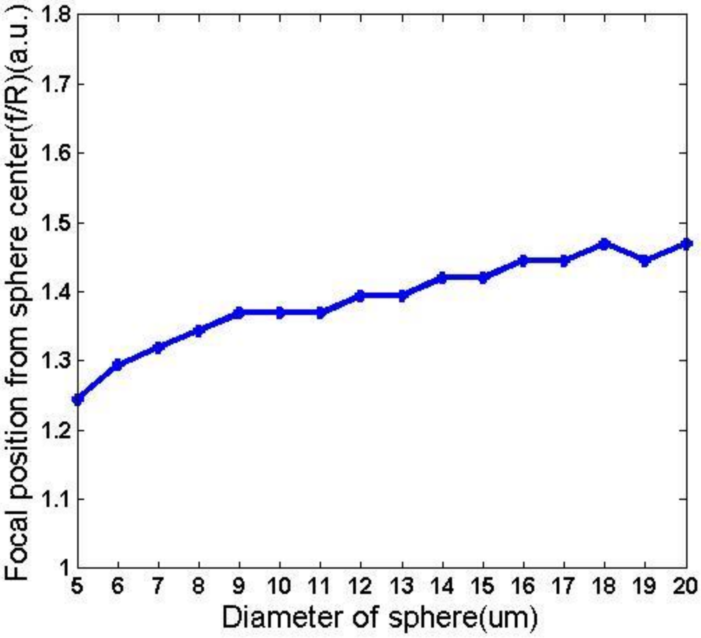

Figure6. 6 The dependence of the focal point on the diameters of the BTG microspheres fully immersed in IPA with λ = 0.55 μm.

The relative refractive index contrast of the barium titanate glass microsphere immersed in IPA (isopropyl alcohol) is $\frac{m}{m_0} = 1.39$. And the focal position for microspheres with the diameters~5-20μm are given in Figure6. 6. As diameter changes from 5 to 20μm, the photonic nanojet moves away from the surface of microsphere from 1.24R to 1.47R, and the maximum intensity of photonic nanojet increases from 122.4 to 621.1, as shown in Figure 6.7.

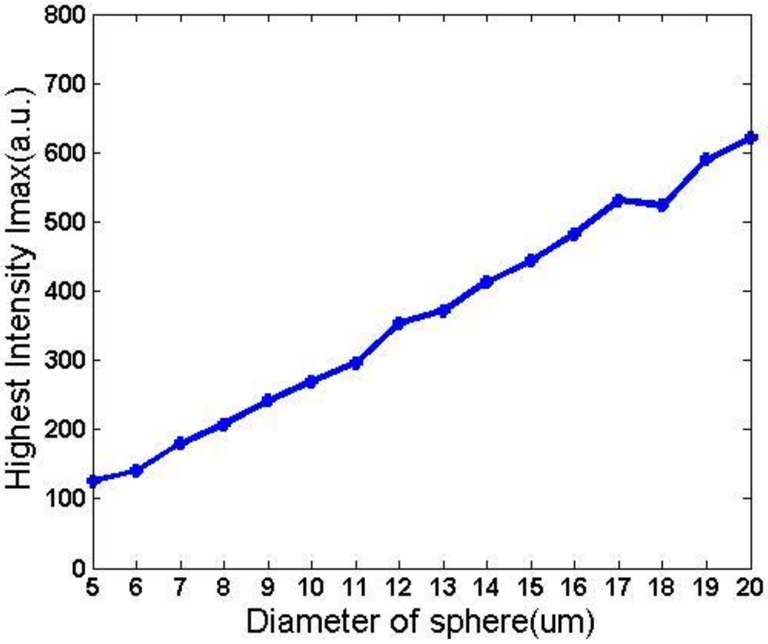

Figure 6.7 The dependence of the maximum intensity of photonic nanojet on the diameters of the BTG microspheres fully immersed in IPA with λ = 0.55 µm.

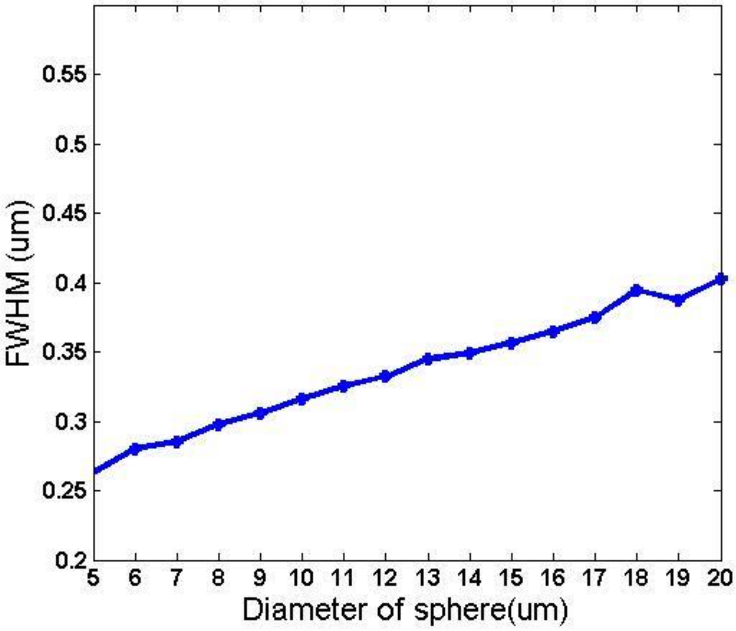

Figure 6.8 The dependence of the resolution on the diameter of the BTG microspheres fully immersed in IPA with λ = 0.55 µm.

The dependence of the resolution on the diameters of the BTG microspheres is illustrated in Figure 6.8. The resolution became deteriorated with increasing diameters of the microspheres, which can be demonstrated by experiment [46].

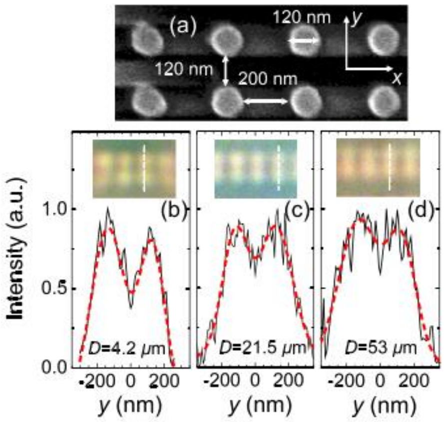

Figure 6.9 (a) SEM image of gold nanoparticle dimers with 120 nm nanoparticles with 120 nm separations. The irradiance profiles were measured along the axis connecting two nanoparticles by BTG microspheres with *m*=1.9 and different diameters is (b) 4.2 µm (c) 21.5 µm (d) 53 µm [46].

The sample is 2D arrays of gold nanoparticle dimers (NPDs) with 120 nm separations in y axis, illustrated in Figure 6.9 (a). The experimental results in Figure 6.9 (b), (c) and (d) show that the microsphere with lower diameters is better. The magnification of the virtual images can be calculated by both geometrical optics Eq.(5.2) and Wang's approximations formula. But the results of these two methods have great differences, as shown in Figure 6.10 (a) and Figure 6.10 (b) respectively. And the experimental results of magnification are measured using microspheres (m=1.9, 2<D<220µm) and nanoparticle dimers (NPD) with 150 nm separations [46].

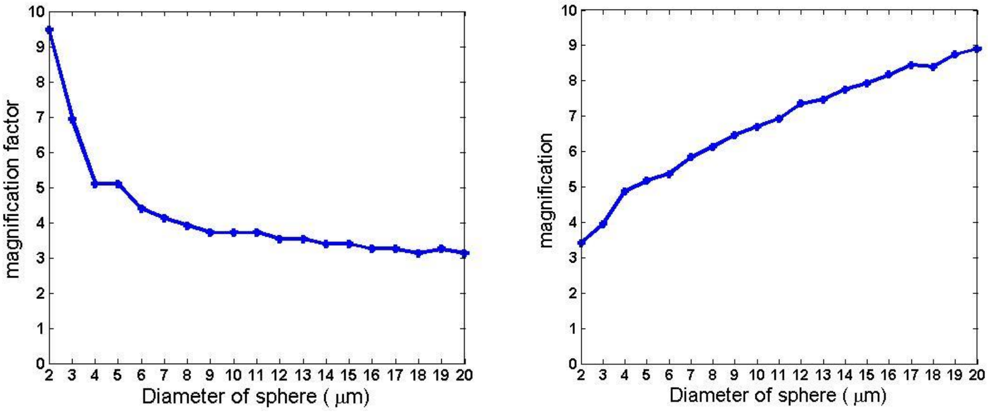

(a) **(b)**

Figure 6.10 The magnification of the virtual images for spheres with diameters in 5–20 μm range according to (a). Geometrical optics Eq(5.2); (b) Wang's approximations formula.

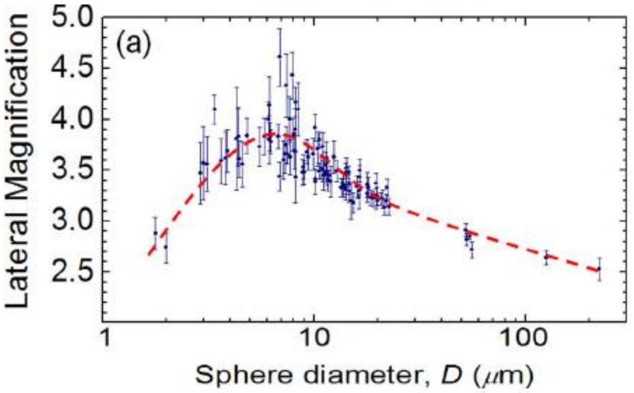

Figure 6.11 Experimental results for magnification measured by using microspheres (m=1.9, 2<D<220μm) and nanoparticle dimers (NPD) with 150 nm separations [46].

According to the experimental results illustrated in Figure 6.11, geometrical optics seems to be a reasonable approximation for microspheres with D>10μm. For smaller microspheres with D~2-6μm, geometrical optics has opposite results and Wang's approximations formula agrees well with the experimental results. And both of geometrical optics and Wang's approximations formula can be used while D~6-10μm.

6.3 Summary

According to Wang's experiment, the corresponding internal and near-external intensity distributions, the location of focal spot and maximum intensity of sample microspheres are computed. The full width at half maximum intensity of photonic nanojet is given and indicates that the diffraction limit is overcome.

The dependence of the focal point, maximum intensity, resolution, magnification on the diameters of the barium titanate glass microspheres fully immersed in isopropyl alcohol are discussed. The simulation results show that he resolution get worse with increasing diameters of the microspheres, which was demonstrated by Darafsheh's experiment. The applicable conditions of geometrical optics and Wang's approximations for magnification calculation have been analyzed. The valid ranges of two methods are investigated.

CHAPTER 7: Image Distortion and Correction of Microsphere

7.1 Image Distortion in Microsphere Nanoscopy

As the measurement technique, one needs not only to study specific experimental method but also accurate data measurements. The microsphere can be considered as a thick lens. The images formed by microsphere are mainly affected by radial distortion, similar to a lens. Radial distortion is a deficiency in straight lines transmission. The effect of radial distortion is that straight lines are bended as general curves and points are moved in the radial direction from their correct position. There are two major types of radial distortion. The first one is barrel distortion, which occurs when points are moved from their correct position towards the center of the image. The second type of radial distortion is pincushion distortion, which occurs when points are displaced further away from the optical axis [94,95,96,97]. From the view of geometrical optics, rays from each point of the object reunite at corresponding points in the image plane, but the magnification varies throughout the plane, as magnification increases with distance from the axis, pincushion occurs as illustrated in Figure 7. 1(b); while magnification decreases with distance from the axis, barrel distortion occurs shown in Figure 7. 1(c).

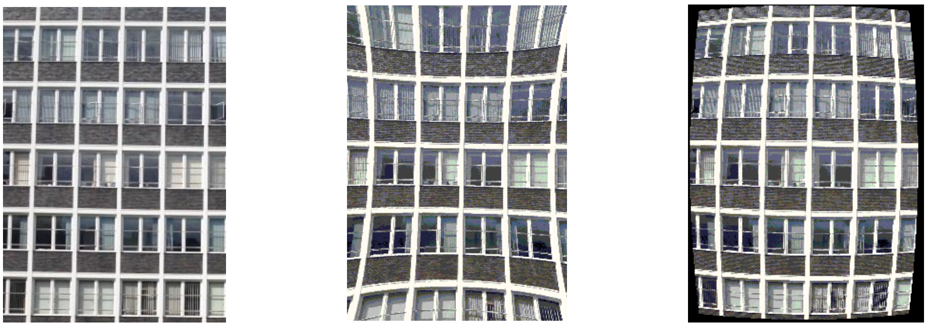

(a) (b) (c)

Figure 7. 1 (a) Original image; (b) Pincushion distortion (c) Barrel distortion

The basic standard model for radial distortion model is an even-order polynomial model [98,99,100]:

$$\begin{bmatrix} x_u - x_c \\ y_u - y_c \end{bmatrix} = L(r) \begin{bmatrix} x_d - x_c \\ y_d - y_c \end{bmatrix} \tag{7.1}$$

where x_d, y_d is the original (distorted) point, x_u, y_u is the corrected (undistorted) point, x_c, y_c is the center of the image, the distance for image point to the center of the image is given by $r = \sqrt{(x_d - x_c)^2 + (y_d - y_c)^2}$. $L(r)$ is radial function which defines the shape of the distortion model，and can be approximated by a Taylor expansion:

$$L(r) = 1 + p_1 r^2 + p_2 r^4 + \ldots\ldots \tag{7.2}$$

where $p = (p_1, p_2, \ldots\ldots)^T$ represents the distortion parameters[101,102,103]. Several tests have demonstrated that approximating the series with only the lower-order component corrects more than the 90% of the radial distortion[104].With using only the first-order radial symmetric distortion parameter p_1, the precision of about 0.1 pixels in the image space can be achieved. So, the radial distortion equation (7.1) is approximated by using only the first term:

$$L(r) = 1 + p_1 r^2 \tag{7.3}$$

The sign of p_1 affects the type of radial distortion. If p_1 is negative, it is a barrel radial distortion. If p_1 is positive, it is a pincushion radial distortion.

Equation (7.1) can be approximated as:

$$\begin{bmatrix} x_u - x_c \\ y_u - y_c \end{bmatrix} = (1 + p_1 r^2) \begin{bmatrix} x_d - x_c \\ y_d - y_c \end{bmatrix} \qquad （7.4）$$

Therefore, by given distorted point coordinates, the undistorted point coordinates can be calculate with using coefficient p_1 . Then, the “undistorted” image point (x_u, y_u) can be mapped from “distorted” image point (x_d, y_d).

7.2 Image Distortion Experiments

Figure 7. 2 shows a schematic of the experimental set-up for microsphere nanoscopy image. The Leica DM2500M upright microscope is used. The optical images of samples can be obtained through the microspheres, which were placed on the sample and immersed in water, as shown in Figure 7. 2. Then the images were captured by a digital CCD camera and stored.

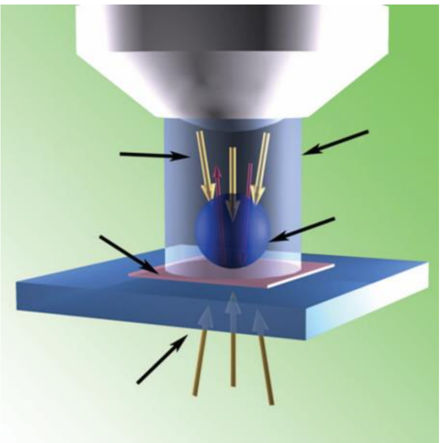

Figure 7. 2. Schematic of the of microsphere nanoscopy image experimental setup.

Experimental images are observed through microspheres, which are placed on different sample. The sample is printed circuit board (PCB) with different separation of patterns and spacing. Figure 7. 3(a) shows the 1μm-width-1μm-spacing pattern under x100 microscope in air, measured with a $BaTiO_3$ microsphere with diameter of 15μm in water, as shown in Figure 7. 3(b). The images show pincushion distortion clearly, visible especially for stripe in the near edge of each image.

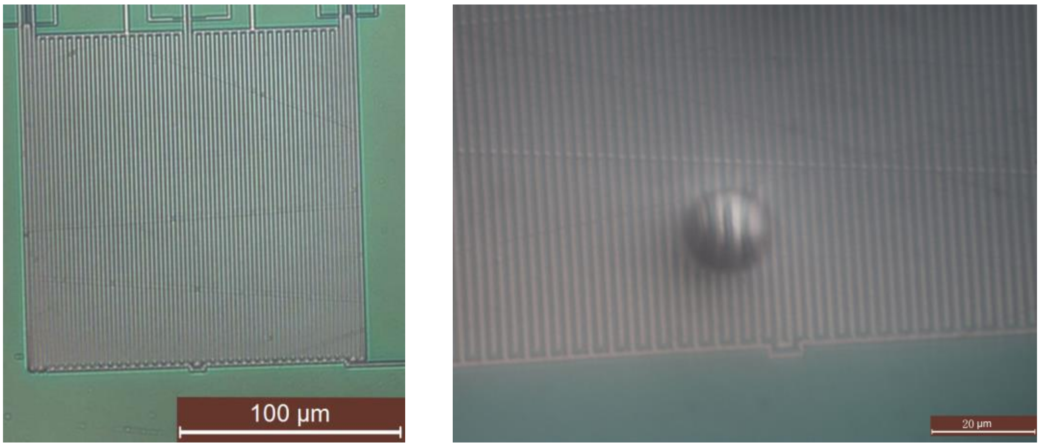

(a) (b)

Figure 7. 3 Experimental images of microscope (x100) (a) 1μm-width-1μm-spacing pattern in air; (b) with a 15μm diameter $BaTiO_3$ microsphere in water.

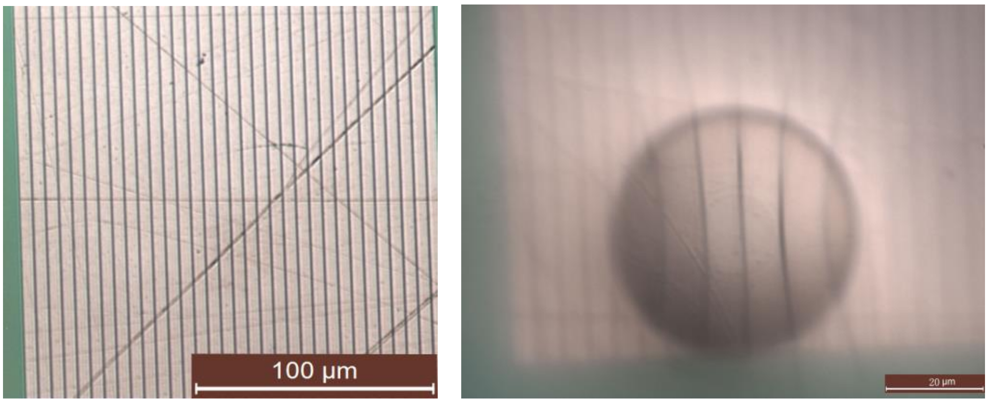

(a) (b)

Figure 7. 4 Experimental images of microscope (x100) (a) 5μm-width-1μm-spacing pattern in air; (b) with a 15μm diameter $BaTiO_3$ microsphere in water.

The images of a 50 μm diameter $BaTiO_3$ microsphere with different patterns are shown in Figure 7. 4 - Figure 7. 6. They are characterized by a strong pincushion distortion which bends the straight lines in near edge of microsphere.

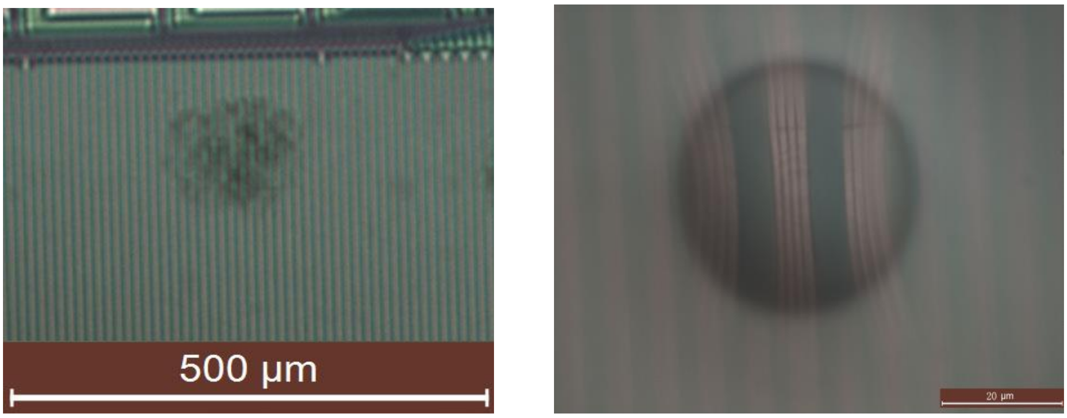

(a) (b)

Figure 7. 5 Experimental images of microscope (x100) (a) 5µm-width-5µm-spacing pattern with inner pattern which could not be observed by optical microscope in air; (b) with a 15µm diameter $BaTiO_3$ microsphere in water.

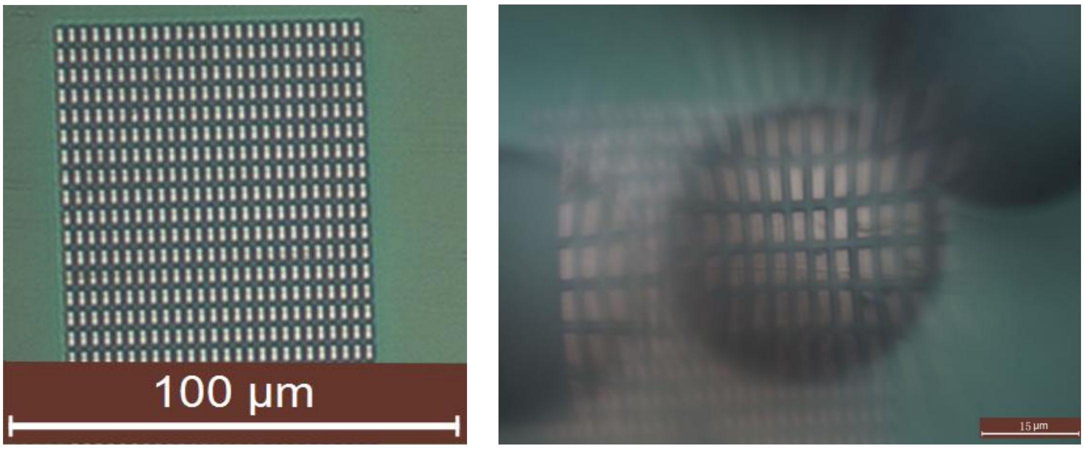

(a) (b)

Figure 7. 6 Experimental images of microscope (x100) (a) 3µm-lenth-1µm-width with 1µm cross spacing pattern in air; (b) with a 15µm diameter $BaTiO_3$ microsphere in water.

7.3 Reduction of Distortion Aberration for Microsphere Image

As described above, the image of microsphere can introduce a pincushion distortion in measurements due to the image magnification increases with the distance from the optical axis. According discussed in section 7.1, each point in the undistorted image corresponds to a point in the distorted image. So using Equation (7.4), the points of the desired image are obtained from corresponding points of the distorted image. The procedure for correcting radial distortion is written by using Matlab, which suppose that the center of distortion is the center of image.

The procedure for correcting radial distortion is written by using Matlab. The “imread” function of MATLAB is used to obtain distorted image data， which is an M-by-N-by-4 array for TIFF files. The center of radial distortion is suppose the center of the image. By using coordinates of distorted point and center point, the undistorted point coordinates can be calculated from Equation (7.4).Then the undistorted image is mapped corresponds to the distorted image. See Appendix A for the Matlab code.

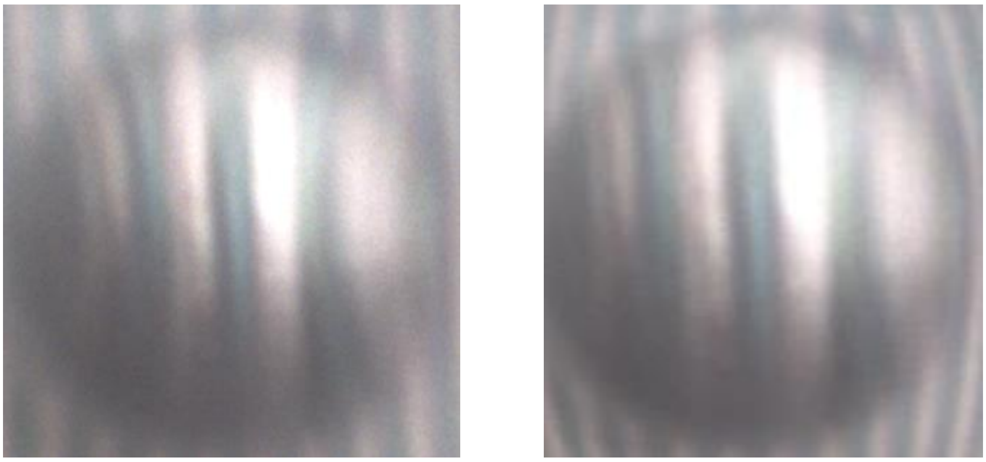

(a) (b)

Figure 7. 7. The pincushion distortion image correction of microsphere corresponding to Figure 7. 3(b). (a) Original image; (b) Corrected image.

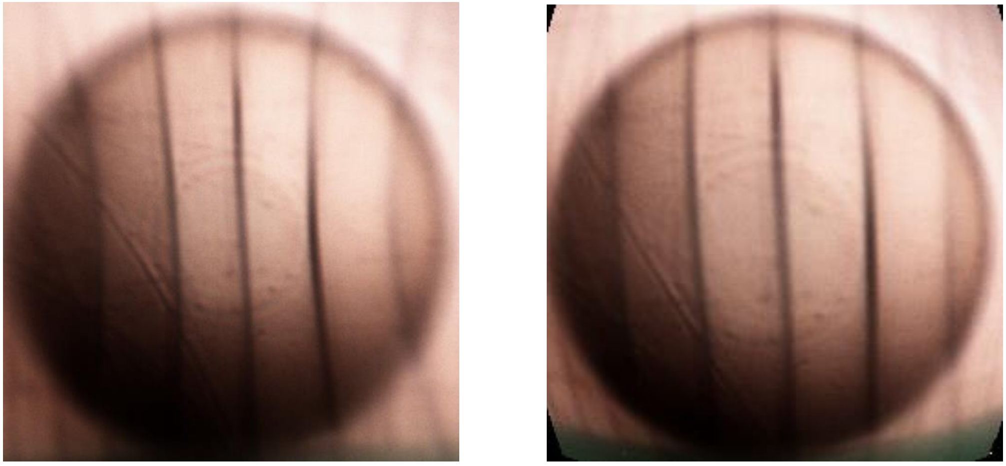

(a) (b)

Figure 7. 8. The pincushion distortion image correction of microsphere corresponding to Figure 7. 4 (b). (a) Original image; (b) Corrected image.

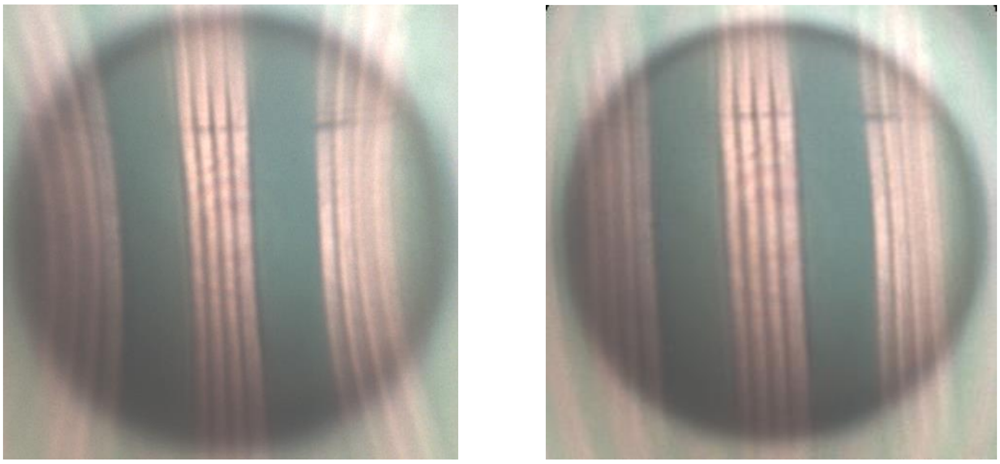

(a) (b)

Figure 7. 9. The pincushion distortion image correction of microsphere corresponding to Figure 7. 5 (b). (a) Original image; (b) Corrected image.

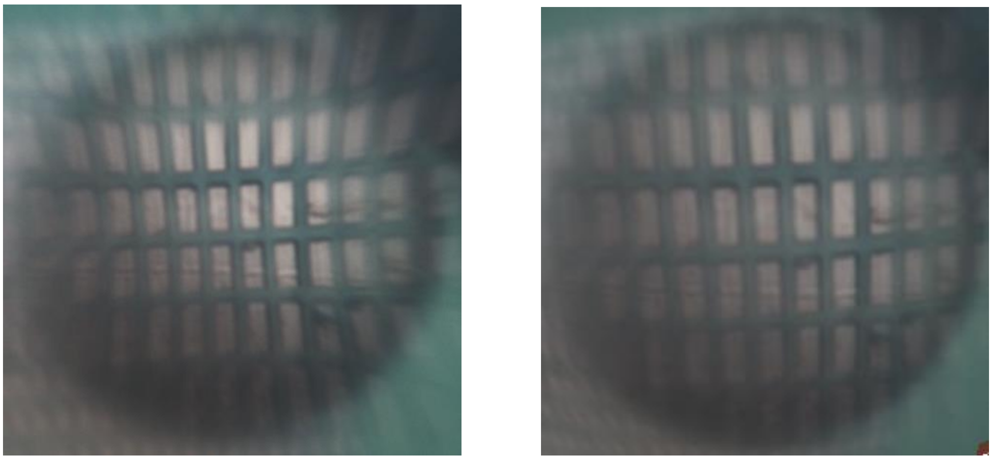
(a) (b)

Figure 7. 10. The pincushion distortion image correction of microsphere corresponding to Figure 7. 6(b). (a) Original image; (b) Corrected image.

Figure 7. 7- Figure 7. 10 illustrate the application of radial distortion model for the pincushion distortion correction. As observed in these Figs, the pincushion distortion of images are properly removed. The stripe of images turn into a straight line in the near edge of each image.

The polynomial model described above provides a way to correct microsphere distortion, which achieves an accuracy of about 0:1 pixels in image space. The amended image can also be used to calibrate the actual magnification and length values of the microsphere, provided highly measurement accuracy. However, there are still many problem need to be solved. In distortion model be a radial function, we assume that the distortion image has square shape and is symmetrical along the center line, the center coordinates of radial distortion is suppose the center of the image. This square shape assumption is satisfied, in practice, for most images. But if the image is not a strict square or symmetry, the center of image is not the center coordinates of radial distortion. The effect of radial distortion reduction correction distortion decrease. The value of radial distortion parameter p_1 is predicted at At the beginning of the calculation, and modified according to the effect of distortion correction. The choice of radial distortion parameter rely on user identifies and intervention. So the automatic method to correct lens radial distortion need to study in the future.

7.4 Summary

The microsphere optical nanoscopy imaging produces a pincushion distortion, which has a significant impact on the image geometry. A radial distortion model is discussed. Some experimental images of microsphere are given which show pincushion distortion clearly. The code for correcting radial distortion is written and applied to correct the pincushion distortion of images.

Conclusion

In this thesis, interactions between microsphere with light wave are analyzed based on Mie theory. The internal and scattered fields are expanded in vector spherical harmonics, the corresponding expansion coefficients are obtained by using boundary conditions. The scattering intensity distributions are calculated, which depend on the size of the sphere, relative refractive index and the incident wavelength. The 3D and 2D intensity distribution of internal and near EM fields of the microsphere is given.

The simulations of internal and near field show that the microsphere can focus light and produce narrow beams. The locations of focal spot are influenced by the refractive index contrast, wavelength and the size of microsphere. If the refractive index is too high, the focus point will be inside the microsphere. The focal spot move toward the center of sphere as wavelength increase or radius of the microspheres decreases. The influence of different refractive indexes on the focal spot is larger than that of wavelength and radius of microsphere.

By increasing the refractive index, the maximum intensity is more intense. For radius $R = 5\mu m$ of microsphere, the properties of nanojet for typical refractive index are discussed: (1). When $m = 1.1$, the nanojet is formed far away from the surface microsphere. The length of the nanojet can be achieved to more than 30λ; (2).When $m = 1.736$, the nanojet is just on the surface of the microsphere with shortening of the nanojet's longitudinal distribution, the maximum intensity of nanojet can be enhanced up to 600 times of the incident intensity. (3).When $m = 1.84$, the photonic nanojet is inside of the microsphere and formed by several small focal spots, which have very narrow width and different intensity. The standing-wave-like interferences, which close to the inner surface of the microsphere. The maximum intensity of the nanojet grows with increasing size of microsphere or decreasing wavelength.

The FWHM of photonic jet, which relate to the resolution of microscopy, have been studied. The FWHM of the photonic nanojet decreases as the refractive index increases, or size of microspheres decrease, or wavelength decreases.

The properties of resolution and magnification with different wavelength, refractive index, microsphere diameter are analyzed by combination of geometrical optics and Mie theory. The influence of refractive index on the magnification is larger that of wavelength and radius of microsphere. Z Wang’s approximate method for the magnification is discussed as the focal point of microsphere is close to object, the value of the magnification appears some fluctuation.

The properties of focal spots, intensity, position, magnifications, et al., are distinct from those predicted by geometrical optics. The relative errors of numerical results between two theories are given.

Two experiments in Ref [3, 46], which are Wang’s and Darafsheh’s experiment, are discussed in a similar manner as Chapter 4 and 5. Internal and near intensity distribution, location of focal spot, maximum intensity, magnification, and FWHM in Wang’s experiment are analyzed. For Darafsheh’s experiment, the features of the focal points, maximum intensity, and the resolution with the different diameters are given,

The pincushion and barrel distortion is introduced when the images are formed by microsphere nanoscope. The distortion aberration for microsphere image is reduced by using the radial distortion model.

Analyzing the numerical results, the work can be used to choose the optimal parameters, such as size of microsphere, wavelength, refractive indices contrast, and create nanojets with desired spatial resolution for microsphere-based microscopy. Also the result can used to design better super-resolution of microsphere-based microscopy.

Proposals for future work:

1. This study investigated the optical super-resolution feature of the single microsphere bases on Mie theory. The properties of multi-sphere or chains of microspheres and their interactions including interferences and image connections, which are similar to a series of microlenses, may be investigated by using Mie theory.
2. As discussions on section 6.2, the valid ranges between geometrical optics and Wang's approximations methods need to be further investigated.
3. It is noted that we assume that microspheres do not have internal resonances in this thesis, the influence of resonances on the super-resolution feature requires further study.

APPENDIX A

Matlab code for correcting radial distortion

```
img_origin = imread('image.tif');

% Change this parameter to improve image quality

p1 =4.0*10^-7;

img_size = size( img_origin );

img_undist = zeros( img_size );

img_undist = uint8( img_undist );

for l0 = 1:img_size(3)

    for l1 = 1:img_size(1)

        y = l1 - img_size(1)/2;

        for l2 = 1:img_size(2)

            x = l2 - img_size(2)/2;

            x1 = round( x * ( 1 + p1 * x * x + p1 * y * y ) );

            y1 = round( y * ( 1 + p1 * x * x + p1 * y * y ) );
```

```
            y1 = y1 +round( img_size(1)/2);
            x1 = x1 + round(img_size(2)/2);
            % if x1 or y1 exceeds boundary£¬ force them to 0(black)
            if x1 < 1 || x1 > img_size(2) || y1 < 1 || y1 > img_size(1)
                img_undist(l1,l2,l0) = 0;
            else
                img_undist(l1,l2,l0) = img_origin(y1, x1,l0);
            end
        end
    end
end
figure(1);
imshow(img_undist);
```

References

1 Hell, S. W. and Wichmann, J., *Breaking the diffraction resolution limit by stimulated emission: stimulated-emission-depletion fluorescence microscopy*, Optics Letters, 19(11): p.780–782, 1994.

2 Lin Li, Wei Guo, Yinzhou Yan, Seoungjun Lee1 and Tao Wang, *Label-free super-resolution imaging of adenoviruses by submerged microsphere optical nanoscopy*, Light: Science & Applications, 2: p104, 2013.

3 Z. Wang, W. Guo, L. Li, B. Luk'yanchuk, A. Khan, Z. Liu, Z. Chen, and M.Hong, *Optical virtual imaging at 50 nm lateral resolution with a white-light nanoscope*, Nature Communications, 2 (218): 2011.

4 Seoungjun Lee, LinLi, *Rapid super-resolution imaging of sub-surface nanostructures beyond diffraction limit by high refractive index microsphere optical nanoscopy* , Optics Communications, 334, 253–257, 2015.

5 S. T. Hess, T. P. K. Girirajan, and M. D. Mason, *Ultra-high resolution imaging by fluorescence photoactivation localization microscopy*, Biophysical journal, 91: p. 4258–72, 2006.

6 M. J. Rust, M. Bates, and X. Zhuang, *Sub-diffraction-limit imaging by stochastic optical reconstruction microscopy (STORM)*, Nature methods, and 3(10): p. 793–795, 2006.

7 Mortimer Abramowitz, *Microscope Basics and Beyond*, New York Microscopical Society.

8 Xu Li, Zhigang Chen and Allen Taflove, Vadim Backman, *Optical analysis of nanoparticles via enhanced backscattering facilitated by 3-D photonic nanojets*, Optics Express, 13(2) p. 526, 2005.

9 Yuri E. Geints, Alexander A. Zemlyanov, and Ekaterina K. Panina, *Photonic nanojet calculations in layered radially inhomogeneous micrometer-sized spherical particles*, 28(8), J. Opt. Soc. Am. B, 2011.

10 Chen Z, Taflove A, Backman V, *Photonic nanojet enhancement of backscattering of light by nanoparticles: a potential novel visible-light ultramicroscopy technique*. Optics Express 12: p.1214–1220, 2004.

11 M. Born and E. Wolf, *Principles of Optics*, 7th Edition, Cambridge University Press, Cambridge, UK, 2003.

12 A. Buxton, *Note on optical resolution*, Philosophical Magazine, 23(154), 440-442, 1937.

13 B. P. Ramsay, E. L. Cleveland, and O. T. Koppius, *Criteria and the intensity epoch slope*, Journal of the Optical Society of America, 31(1), 26-33, 1941.

14 A. J. den Dekker and A. van den Bos, *Resolution: a survey*, Journal of the Optical Society of America A, 14(3), 547-557, 1997.

15 Lord Rayleigh, *Investigations in optics, with special reference to the spectroscope*, Philosophical Magazine, 8(49): p.261-274 ,1879.

16 E. Abbe, *Beitrage zur theorie des mikroskops und der mikroskopischen wahrnehmung*, Archiv fur Mikroskopische Anatomie, 9(1): p.413-418, 1873.

17 C. M. Sparrow, *On spectroscopic resolving power*, Astrophysical Journal, 44(2): p.76-86, 1916.

18 W. V. Houston, *A compound interferometer for fine structure work*, Physical Review, 29(3): 478-484, 1927.

19 Hell, S. W. *Strategy for far-field optical imaging and writing without diffraction limit*. Physics Letters A, 326(1–2):140–145, 2004.

20 Rizzoli, S. O., Westphal, V., Lauterbach, M. A., Kamin, D., and Hell, S. W. *Synaptic vesicle recycling investigated by super-resolution microscopy*. Journal of Neurochemistry, 108 (Suppl. 1):55–56, 2009

21 Klar, Thomas A., Stefan W. Hell, *Sub-diffraction resolution in far-field fluorescence microscopy,* Optics Letters 24 (14): 954–956， 1999.

22 Peter Dedecker, Johan Hofkens, and Jun-ichi Hotta, *Diffraction-unlimited optical microscopy,* materials today, 11: Supplement, p.12–21, 2008.

23 Westphal, V., et al., *Lateral resolution of 28 nm (λ /25) in far-field fluorescence microscopy*, Applied Physics B, 77: p 377-380, 2003.

24 Donnert, G., et al., *Macromolecular-scale resolution in biological fluorescence microscopy*, Proc. Natl. Acad. Sci. USA 103: p.11440 –11445, 2006.

25 Harke, B., Keller, J., Ullal, C. K., Westphal, V., Sch¨onle, A., and Hell, S. W. *Resolution scaling in STED microscopy*. Optics Express, 16(6):4154–4162, 2008.

26 Meyer, L., Wildanger, D., Medda, R., Punge, A., Rizzoli, S. O., Donnert, G., and Hell, S. W. *Dual-color STED microscopy at 30-nm focal-plane resolution*. Small, 4(8):1095–1100, 2008.

27 Moneron, G. and Hell, S. W. *Two-photon excitation STED microscopy*. Optics Express, 17(17):14567–14573, 2009.

28 Rittweger, E., Han, K. Y., Irvine, S. E., Eggeling, C., and Hell, S. W. *STED microscopy reveals crystal colour centres with nanometric resolution*. Nature Photonics, 3(3):144–147, 2009.

29 Synge, E. H., *A suggested method for extending the microscopic resolution into the ultramicroscopic region*, The London, Edinburgh, and Dublin Philisophical Magazine and Journal, 1928.

30 Ash EA, Nicholls G, *Super-resolution aperture scanning microscope*, Nature, 237:510–3, 1972.

31 Lewis, A., Isaacson, M., Harootunian, A., and Murray, A., *Development of a 500A spatial resolution light microscope*, Ultramicroscopy, 13: p.227, 1984.

32 Vigoureux, J., M.,Girard, C., and Courjon, D., *General principles of scanning tunnelling optical microscopy*, Opt. Lett. 14: p.1039, 1989.

33 Betzig, E., Finn, P. L., and Weiner, J. S., *Combined shear force and near-field scanning optical microscopy*, Appl. Phys. Lett. 60: p.2484, 1992.

34 Pohl, D. W., and Novotny, L., *Near-field optics: Light for the world of nano,* J. of Vac. Sci. and Tech. B, 12: p.1441, 1994.

35 Veerman, J. A., Otter, A. M., Kuipers, L., and van Hulst, N. F., *High definition aperture probes for near-field optical microscopy fabricated by focused ion beam milling*, Appl. Phys. Lett. 72: p.3115, 1998.

36 Dunn, R. C., *Near-field scanning optical microscopy,* Chem. Rev. 99: p.2891, 1999.

37 Frey, H. G., Keilmann, F., Kriele, A., and Guckenberger, R., *Enhancing the resolution of scanning near-field optical microscopy by a metal tip grown on an aperture probe,* Appl. Phy. Lett. 81: p.5030, 2002.

38 Esmann M, Becker SF, da Cunha BB, Brauer JH, Vogelgesang R, Groß P, Lienau C. *K-space imaging of the eigenmodes of sharp gold tapers for scanning near-field optical microscopy*. Beilstein J Nanotechnol, 4: p.603–10, 2013.

39 Toshiharu Saiki and Yoshihito Narita, *Recent Advances in Near-field Scanning Optical Microscopy*, JSAP International, 5, 2002.

40 T. Pangaribuan, K. Yamada, S. Jiang, H. Ohsawa and M. Ohtsu, *Reproducible Fabrication Technique of Nanometric Tip Diameter Fiber Probe for Photon Scanning Tunneling Microscope*, Jap. J. Appl. Phys. 31: L1302, 1992.

41 S. Mononobe and M. Ohtsu, *Development of a fiber used for fabricating application oriented near-field optical probes*, IEEE Photon.Technol. Lett. 10, p.99, 1998.

42 A. L. Lereu , A. Passian and Ph. Dumas, *Near field optical microscopy: a brief review*, International Journal of Nanotechnology, 9(3): p.488-501, 2012.

43 Seoungjun Lee, Lin Li, Zengbo Wang, Wei Guo, Yinzhou Yan, and Tao Wang , *Immersed transparent microsphere magnifying sub-diffraction-limited objects*, Applied Optics, Vol. 52, No. 30, p.7266-7270, 2013 ,

44 Seoungjun Lee, Lin Li, Yacob Ben-Aryeh, Zengbo Wang, and Wei Guo, *Overcoming the diffraction limit induced by microsphere optical nanoscopy,* J. Opt. 15, 125710, 2013.

45 Xiang Hao, Cuifang Kuang, Xu Liu, Haijun Zhang, and Yanghui Li, *Microsphere based microscope with optical super-resolution capability*, Applied Physics Letters, 99: p.203102, 2011.

46 A. Darafsheh, et al. *Optical super-resolution by high-index liquid immersed microspheres*, Appl. Phys. Lett., 101: p.141128, 2012.

47 L.A. Krivitsky, et al. *Locomotion of microspheres for super-resolution imaging, Scientific Reports*, 3, p.3501, 2013.

48 A. Darafsheh, et al. *Advantages of microsphere-assisted superresolution imaging technique over solid immersion lens and confocal microscopies,* Appl. Phys. Lett., 104: 061117, 2014.

49 Y. Yan, et al. *Microsphere-coupled scanning laser confocal nanoscope for sub-diffraction limited imaging at 25 nm lateral resolution in the visible spectrum*, ACS Nano, 8: p.1809–1816, 2014.

50 Kenneth W. Allen, Navid Farahi, Yangcheng Li, et al. *Super-Resolution Imaging by Arrays of High-Index Spheres Embedded in Transparent Matrices*, National Aerospace and Electronics Conference (NAECON), Dayton, Ohio, 2014.

51 Arash Darafsheh, Consuelo Guardiola, et al, *Optical super-resolution imaging by high-index microspheres embedded in elastomers*, Optics Letters, 40(1): 2015.

52 Yubo Duan, George Barbastathis, and Baile Zhang, *Classical imaging theory of a microlens with super-resolution*, Optics Letters, 38(16): 2013.

53 Alexander Heifetz, Jamesina J. Simpson, *Subdiffraction optical resolution of a gold nanosphere located within the nanojet of a Mie-resonant dielectric microsphere,* Optics Express , 15(25): 2007.

54 A. M. H. Wong and G. V. Eleftheriades, *An optical super-microscope for far-field realtime imaging beyond the diffraction limit,* Scientific reports, vol. 3, p. 1715, 2013.

55 Sylvain Lecler, *Properties of a three-dimensional photonic jet,* Optics Letters, 30(19): 2005.

56 Alexander Heifetz, Kevin Huang, *Experimental confirmation of backscattering enhancement induced by a photonic jet*, Applied Physics Letters 89: p.221118, 2006.

57 Alexis Devilez, Brian Stout, Nicolas Bonod, Evgeny Popov, *Spectral analysis of three-dimensional photonic jets,* Optics Express, 16(18): p.14200-14212, 2008.

58 Mie, G. Beitrage zur *Optik trüber Medien speziell kolloidaler Metallösungen,* Ann. Physik 25: p.377–445, 1908.

59 Brillouin L., *Light scattering cross section of spheres for Electromagnetic waves*, J. Applied Physics, 20, pp. 1110-1125, 1949.

60 Kerker, M., *The scattering of light and other electromagnetic radiation*, New York: Academic, 1969.

61 Tam, W. G., and Corriveau, R., *Scattering of electromagnetic beams by spherical objects*, J. Opt. Soc. Am., 68, pp.763-767, 1978.

62 H. C. van de Hulst. *Light scattering by small particles,* Dover Publications, New York, 1957.

63 J. A. Stratton, *Electromagnetic theory,* McGraw-Hill, New York, 1941.

64 Craig F. Bohren，Donald R. Huffman, *Absorption and Scattering of Light by Small Particles*, John Wiley & Sons，Inc. 1983.

65 Morita N, Tanaka T, Yamasaki T, et al. *Scattering of a beam wave by a spherical object*, IEEE Trans. Antennas Propagat., 1968, 16: 724-727.

66 L. W. Davis, *Theory of electromagnetic beams*, Phys. Rev. A 19, 1177 - 1179, 1978.

67 E. Almaas and I. Brevik, *Radiation forces on a micrometer sized sphere in an evanescent field*, J. Opt. Soc. Am. B 12, p.2429–2438, 1995.

68 D. W. Mackowski, *Calculation of total cross sections of multiple sphere clusters*, J. Opt. Soc. Amer. A, 11: p.2851－2861, 1994.

69 R. T. Wang and H. C. van de Hulst, *Rainbows: Mie computations and the Airy approximation*, Appl. Opt. 30, 106-117, 1991.

70 W. C. Mundy, J. A. Roux, and A. M. Smith, *Mie scattering by spheres in an absorbing medium*, J. Opt. Soc. Am. 64, 1593–1597, 1974.

71 P. Chylek and J. Zhan, *Absorption and scattering of light by small particles: the interference structure*, Appl. Opt. 29, 3984, 1990.

72 Hong Du, *Mie-scattering calculation*, Applied Optics, Vol. 43, No. 9, p.1952-1956 2004.

73 W. J. Wiscombe, *Improved Mie scattering algorithms*, Appl. Opt. 19, 1505–1509, 1980.

74 Daniel S. Benincasa, Peter W. Barber, Jian-Zhi Zhang, Wen-Feng Hsieh, and Richar K. Chang, *Spatial distribution of the internal and near-field intensities of large cylindrical and spherical scatterers*, Applied Optics ,Vol. 26, No. 7 , p.1348-1356,1987.

75 Sylvain Lecler, Yoshitate Takakura, Patrick Meyrueis, *Properties of a three-dimensional photonic jet,* Optics Letters, 30(19): p.2641, 2005.

76 Patrick Ferrand, JeromeWenger, *Direct imaging of photonic nanojets,* Optics Express, 16(10): p.6930, 2008.

77 A. Heifetz, S.-C. Kong, A. V. Sahakian, A. Taflove, and V. Backman, *Photonic nanojets*, Journal of Computational and Theoretical Nanoscience, 6(9), 1979-1992, 2009.

78 A. V. Itagi and W. A. Challener, *Optics of photonic nanojets*, Journal of the Optical Society of America A, 22(12), 2847-2858, 2005.

79 Y. E. Geints, A. A. Zemlyanov, and E. K. Panina, *Controlling the parameters of photon nanojets of composite microspheres*, Optics and Spectroscopy, 109(4), 590-595, 2010.

80 Y. E. Geints, E. K. Panina, and A. A. Zemlyanov, *Control over parameters of photonic nanojets of dielectric microspheres*, Optics Communications, 283(23), 4775-4781 , 2010.

81 H. Ding, L. Dai, and C. Yan, *Properties of the 3D photonic nanojet based on the refractive index of surroundings*, Chinese Optics Letters, 8(7), 706-708, 2010.

82 Y. E. Geints, A. A. Zemlyanov, and E. K. Panina, *Photonic jets from resonantly excited transparent dielectric microspheres,* Journal of the Optical Society of America B, 29(4), 758-762, 2012.

83 C. C. Lam, P. T. Leung, and K. Young, *Explicit asymptotic formulas for the positions, widths, and strengths of resonances in Mie scattering*, Journal of the Optical Society of America B, 9(9), 1585-1592, 1992.

84 Michael I. Mishchenko , Andrew A. Lacis, *Manifestations of morphology-dependent resonances in Mie scattering matrices*, Applied Mathematics and Computation 116 167-179,2000.

85 A. Devilez, N. Bonod, J. Wenger, D. Gérard, B. Stout, H. Rigneault, and E. Popov, *Three-dimensional subwavelength confinement of light with dielectric microspheres,* Optics Express, 17(4), 2089-2094, 2009.

86 Y. E. Geints, A. A. Zemlyanov, and E. K. Panina, *Photonic nanojet effect in multilayer micrometer-sized spherical particles*, Quantum Electronics, 41(6), 520-525, 2011.

87 K. Karrai, X. Lorenz, and L. Novotny, *Enhanced reflectivity contrast in confocal solid immersion lens microscopy*, Applied Physics Letters, 77(21): p.3459-3461, 2000.

88 W. V. Houston, *A compound interferometer for fine structure work*, Physical Review, 29(3), 478-484, 1927.

89 N. Arnold, *Theoretical description of dry laser cleaning*, Applied Surface Science, 208: p.15–22, 2003.

90 Wang, Z. and L. Li, *White-light microscopy could exceed 50 nm resolution*, Laser Focus World, 47(7): p. 61-64, 2011.

91 Ye, R.; Ye, Y.; Ma, H. F.; Ma, J.; Wang, B.; Yao, J.; Liu, S.; Cao, L.; Xu, H.; Zhang, J. *Experimental Far-Field Imaging Properties of a ~5 μm Diameter Spherical Lens*, Opt. Lett., 38, 1829–1831, 2013.

92 Guo, H.; Han, Y.; Weng, X.; Zhao, Y.; Sui, G.; Wang, Y.; Zhuang, S. *Near-Field Focusing of the Dielectric Microsphere with Wavelength Scale Radius,* Opt. Express. 21, 2434–2443, 2013.

93 Arash Darafsheh, *Optical super-resolution and periodical focusing effects by dielectric microspheres*, PhD thesis, The University of North Carolina,2013

94 Bukhari, F., Dailey, M., *Robust radial distortion from a single image,* Lecture Notes in Computer Science 6454, p.1120, 2010.

95 Brown, D., *Close-range camera calibration,* Photogrammetric Engineering 37, 855－866. 1971.

96 Hartley, R.I., Zisserman, A., *Multiple view geometry in computer vision,* Cambridge University Press, 2004.

97 McGlone, C., *Manual of Photogrammetry,* forthed. American Society of Photogrammetry, 1980.

98 Miguel Alemán-Flores, Luis Alvarez,et al *Line detection in images showing significant lens distortion and application to distortion correction,* Pattern Recognition Letters, 36: p.261–271,2014.

99 Alvarez, L., Gomez, L., Sendra, R., *Accurate depth dependent lens distortion models: an application to planar view scenarios,* Journal of Mathematical Imaging and Vision, 39: p.75–85, 2011.

100 Chien-Yue Chen, Wei-Chia Su, Yi-Fan Wang, Cheng-Hung Chen, *Reduction of distortion aberration in imaging systems by using a microlens array,* Optics Communications, 283, p. 2798－2802, 2010.

101 Bukhari, F., Dailey, M., *Automatic radial distortion estimation from a single image,* Journal of Mathematical Imaging and Vision, 45, p.31-45, 2012.

102 Devernay, F., Faugeras, O., *Straight lines have to be straight,* Machine Vision and Applications, 13, p.14-24, 2001.

103 Duda, R.O., Hart, P.E., *Use of the Hough transformation to detect lines and curves in pictures*, Communications of the ACM, 15, p.11-15, 1972.

104 C.C. Slama, *Manual of Photogrammetry,* Fourth Edition, American Society of Photogrammetry and Remote Sensing, Falls Church, Virginia, USA, 1980.